

PLASMA FLOW CONTROL FOR NOISE REDUCTION  
ON A G550 NOSE LANDING GEAR:  
THE DEVELOPMENT OF A PLASMA FAIRING

A Prospectus for a Dissertation

Submitted to the Graduate School  
of the University of Notre Dame  
in Partial Fulfillment of the Requirements  
for the Degree of

Doctor of Philosophy

by  
Michael C. Wicks

---

Flint O. Thomas, Director

Graduate Program in Aerospace and Mechanical Engineering

Notre Dame, Indiana

December 2015

© Copyright by  
Michael C. Wicks  
2015  
All Rights Reserved

## CONTENTS

FIGURES . . . . .	iii
TABLES . . . . .	iv
CHAPTER 1: INTRODUCTION . . . . .	1
1.1 Motivation . . . . .	3
1.2 Theory of Aeroacoustics . . . . .	3
1.3 Landing Gear . . . . .	7
1.3.1 Geometry . . . . .	8
1.3.2 Noise Sources . . . . .	8
1.4 Literature Review . . . . .	12
1.4.1 Single Cylinder Plasma Flow Control . . . . .	12
1.4.2 Tandem Cylinders Plasma Flow Control . . . . .	13
1.4.3 Shock Strut-Torque Arm Assembly Plasma Flow Control . . . . .	14
CHAPTER 2: EXPERIMENTAL APPROACH . . . . .	17
2.1 Experimental Objective . . . . .	17
2.2 Experimental Facility . . . . .	17
2.3 Notre Dame G550 Nose Landing Gear Model . . . . .	19
2.4 Microphone Measurements . . . . .	19
2.5 Flow Visualization . . . . .	20
2.6 Data Acquisition . . . . .	21
2.7 Current Results . . . . .	23
2.7.1 Wind Tunnel Background Noise Characterization . . . . .	23
2.7.2 Far field check . . . . .	23
2.7.3 Comparison with UFAFF Measurements . . . . .	25
2.7.4 Effects of Tripping . . . . .	28
2.7.5 Preliminary Acoustic Assesment . . . . .	28
CHAPTER 3: OBJECTIVES AND FUTURE WORK . . . . .	35
3.1 Research Objectives . . . . .	35
3.2 Proposed Future Work . . . . .	35
3.2.1 Plasma Actuator Configuration . . . . .	36
3.2.2 Noise Reduction Assessment . . . . .	36
3.3 Conclusion . . . . .	37

BIBLIOGRAPHY . . . . .	38
------------------------	----

## FIGURES

1.1	Photograph of Gulfstream 550 Nose Landing Gear. . . . .	8
1.2	Schematic view of Gulfstream 550 Nose Landing Gear components [9].	9
1.3	Flow Visualization of single cylinder in cross-flow with Spanwise and PSVG plasma actuators. . . . .	13
1.4	Flow Visualization of tandem cylinders in cross-flow with Spanwise and PSVG plasma actuators. . . . .	15
1.5	Flow Visualization of torque-arm assembly in cross-flow with Spanwise plasma actuators. . . . .	16
2.1	ND G550 model with and without plasma fairing installed. . . . .	18
2.2	Schematic of the polar array. . . . .	20
2.3	Photograph of the polar array installed in the ND AWT. . . . .	21
2.4	Photograph of the experimental setup for high speed flow visualization.	22
2.5	Representative far field noise level with and without Baseline 1 model installed at $\theta = 90^\circ$ . . . . .	24
2.6	Far field measurement analysis for $d = 48$ in and $d = 59$ in at $\theta = 90^\circ$	25
2.7	Comparison of far field noise level at UFAFF and ND AWT facilities at $\theta = 90^\circ$ . . . . .	27
2.8	Comparison of design of the NASA G550 and ND G550 model geometries. . . . .	27
2.9	Comparison of far field noise level with and without the presence of a trip at $\theta = 90^\circ$ . . . . .	29
2.10	1/3-octave band sound pressure level for various plasma actuator configurations. . . . .	32
2.11	Overall sound pressure level at key polar array locations. . . . .	33
2.12	Landing gear flow visualization orthogonal (left) and at $45^\circ$ (right). .	34

## TABLES

1.1	Physical mechanisms of flow-generated noise. . . . .	12
2.1	Data acquisition parameters. . . . .	22

## CHAPTER 1

### INTRODUCTION

Air travel in the U.S. is steadily growing due in part to an improving economy. Landings and take-offs at airports with FAA-operated and -contracted towers are forecasted to increase from 48.9M to 59.9M or 22.5% between 2015 and 2035 [20]. With the continuing growth of air traffic, additional airports are being built and existing airports are expanding. As this occurs, it is hard to ignore a significant byproduct: the increase in noise caused by aircraft.

The steady encroachment of airports is especially problematic in metropolitan areas, where aircraft noise can negatively impact quality of life. While this issue began as a public interest initiative, a recent study has found a statistically significant link between aircraft noise and cardiovascular disease [2]. Correia et al. looked at 89 of the largest airports across the U.S., and found that, even when controlling for other environmental factors, a 10 dB increase in noise was associated with a 3.5 % increase in hospital admissions in patients 65 years and older. Additional studies are ongoing, especially in the UK and EU, examining other potential adverse health effects such as delayed cognitive development in children [7]. In light of these studies, it is clear: engineers and scientists have an ethical imperative to ensure the safety of technology.

Progress is being made in the field of aeroacoustics. In general, aircraft have become “quieter”, especially due to the widespread adoption of the turbofan jet engine. With the reduction of jet engine noise, aircraft noise has come to a level comparable to that of the airframe on approach and landing conditions [4]. The airframe is the

new “lower noise barrier” of aircraft noise production. Efforts have been taken to quantify airframe noise. In a study by Gibson, flyover noise measurements were performed identifying landing gears and high-lift devices as the two major contributors to airframe noise [8].

In addition to these efforts, several government initiatives have been launched to advance quiet aircraft technology. In the EU, European Visions 2020 called for a reduction of “subjective noise impact by half” (minus 10 dB) per operation by 2020 relative to year 2000 level technology [1]. While in the US, the national Advanced Subsonic Transport (AST) and Quiet Aircraft Technology research programs have even more stringent milestones.

Due in part to these initiatives, several noise reduction technologies have been applied to aircraft landing gear. Dobrzynski et al. studied the effect of solid, streamlined add-on fairings to various areas of main and nose landing gears [5]. While these fairings were effective at reducing mid and high frequency noise levels, they had the drawback of increasing noise in the low frequency range. This study and those like it revealed that solid fairings acted to increase local flow velocity and thus noise from adjacent gear components.

The findings of work with solid fairing suggested the possibility that a porous fairing could streamline geometry while preventing the increase of local flow velocity. Ravetta et al. demonstrated the effects of elastic membrane fairings on reducing sideline noise for a 26%-scale Boeing 777 main landing gear [21]. They observed an average of 2 dB decrease over all frequencies and a 5 dB peak decrease at high-frequency ( $> 10$  kHz). This was achieved through the application of fairings to main strut and brace locations. An elastic-membrane lower truck fairing was also examined yielding similar results.

These technologies share a common approach in that they each utilize passive flow control. The present work is focused on the use of active flow control via di-

electric barrier discharge (DBD) plasma actuation. Applications of this technology on geometries relevant to aircraft landing gear, suggest a potential advantage in this approach due to the variety of possible actuation strategies available. Examples are presented in the literature review section.

### 1.1 Motivation

The present work is motivated to reduce noise produced by aircraft landing gear by flow control via application of DBD plasma actuators. To this end, experiments will be performed to 1) better understand the noise generation mechanisms present on aircraft landing gear, thereby aiding in the formation of flow control strategies, and 2) take steps toward the development of “plasma fairing” technology, which is a device that can be retrofitted to existing aircraft landing gears with the purpose of reducing noise production.

In this chapter, the physics of airframe noise production is discussed. The structure of Aircraft landing gear is presented. Areas of noise contribution are considered and the underlying physical mechanisms are identified. Finally, the literature is reviewed with respect to the application of plasma flow control to increasingly complex geometries pertaining to aircraft landing gear.

### 1.2 Theory of Aeroacoustics

To arrive at a viable flow control strategy, it is useful to first review the underlying physics. The modern theory of aeroacoustics, that is sound generated by aerodynamic means, is based on James Lighthill’s so-called acoustic analogy. He states that sound generated in a fluid flow is only important in regions of turbulent fluctuations [12]. Based on this assumption, the Navier-Stokes Equation and isentropic equation of state in indicial notation are

$$\frac{\partial \rho}{\partial t} + \frac{\partial(\rho u_i)}{\partial x_i} = 0, \quad (1.1)$$

$$\frac{\partial(\rho u_i)}{\partial t} + \frac{\partial(\rho u_i u_j + P_{ij})}{\partial x_j} = 0, \quad (1.2)$$

$$c_o^2 = \frac{\partial p}{\partial \rho}|_{s=const.} = \frac{p'}{\rho'} \quad (1.3)$$

where

$$P_{ij} = p' \delta_{ij} - \sigma_{ij}. \quad (1.4)$$

$P_{ij}$  is the total stress tensor,  $\rho$  is the fluid density,  $u$  is the local velocity vector,  $p$  is the pressure and  $c_o$  is the local speed of sound. Also,  $p' = p - p_o$  and  $\rho' = \rho - \rho_o$  represent the fluctuating pressure and density relative to the mean values, respectively. After assuming sufficiently small fluctuations, equations 1.1 and 1.2 can be linearized yielding the classical Lighthill's equation

$$\frac{\partial^2 \rho}{\partial t^2} - c_o^2 \nabla^2 \rho = \frac{\partial^2 T_{ij}}{\partial x_i \partial x_j}, \quad (1.5)$$

where the source term  $T_{ij}$  is known as Lighthill's turbulence stress tensor

$$T_{ij} = \rho u_i u_j + P_{ij} - c_o^2 (\rho - \rho_0) \delta_{ij}, \quad (1.6)$$

and where  $\delta_{ij}$  is the Kronecker delta which is defined as,

$$\delta_{ij} = \begin{cases} 1 & \text{if } i = j \\ 0 & \text{if } i \neq j \end{cases}. \quad (1.7)$$

For the special case of high Reynolds number, incompressible flow, both the den-

sity fluctuations and the viscous stresses are negligible, reducing the Lighthill stress tensor to

$$T_{ij} \approx \rho_0 u_i u_j. \quad (1.8)$$

Equation 1.5 can be solved and formulated in terms of  $p'$  by combining with equation 1.3 giving

$$p' = c_o^2 \rho' = \frac{1}{4\pi} \frac{\partial^2}{\partial x_i \partial x_j} \int_V \frac{T_{ij}}{r} dV, \quad (1.9)$$

where  $V$  represents the volume of the region of interest, and  $r$  represents the distance to the acoustic source.

In 1955, Lighthill's analogy was extended to account for the presence of solid boundaries within the turbulent flow region [3]. The general solution to this equation is

$$\begin{aligned} p' = & \underbrace{\frac{1}{4\pi} \frac{\partial^2}{\partial x_i \partial x_j} \int_V \left[ \frac{T_{ij}}{r} \right] dV}_I - \underbrace{\frac{1}{4\pi} \frac{\partial}{\partial x_j} \int_S \left[ \frac{P_{ij} + \rho u_i u_j}{r} \right] n_i dS}_{II} \\ & + \underbrace{\frac{1}{4\pi} \frac{\partial}{\partial t} \int_S \left[ \frac{\rho u_i}{r} \right] n_i dS}_{III}, \end{aligned} \quad (1.10)$$

where  $S$  represents the control surface bounding the volumetric region of interest [11]. Equation 1.10 forms the basis of airframe noise generation by including the effects of reflection and diffraction of acoustic waves at the boundaries.

To illustrate the nature of the acoustic source terms on the right hand side of equation 1.10, an order-of-magnitude scaling analysis is performed with the purpose of determining the radiation patterns of the hypothetical acoustic source with respect to flow speed,  $U_o$ , and propagation distance,  $r$ . Lighthill conveniently used a subsonic, turbulent isothermal jet to provide a physical application for which characteristic

length, frequency, pressure, and velocity scales can be defined [18]. Substituting the pertinent characteristic scales yields the following order-of-magnitude approximations for the components of the acoustic source term:

$$\int_V dV \propto D^3 \quad (1.11)$$

$$T_{ij} \propto \rho_o U_o^2 \quad (1.12)$$

$$\frac{\partial}{\partial x_i} = \frac{\partial}{c_o \partial t} \propto \frac{f}{c_o} \propto \frac{U_o}{c_o D} \quad (1.13)$$

Equations 1.11 - 1.13 are then utilized to replace the source terms in equation 1.10, resulting in the following:

$$I : \frac{1}{4\pi} \frac{\partial^2}{\partial x_i \partial x_j} \int_V \left[ \frac{T_{ij}}{r} \right] dV \propto \left( \frac{U_o}{c_o D} \right)^2 (D^3) \left( \frac{\rho_o U_o^2}{r} \right) \propto \frac{U_o^4}{r}, \quad (1.14)$$

$$II : \frac{1}{4\pi} \frac{\partial}{\partial x_j} \int_S \left[ \frac{P_{ij} + \rho u_i u_j}{r} \right] n_i dS \propto \left( \frac{U_o}{c_o D} \right) \left( \frac{\rho_o U_o^2}{r} \right) (D^2) \propto \frac{U_o^3}{r}, \quad (1.15)$$

$$III : \frac{1}{4\pi} \frac{\partial}{\partial t} \int_S \left[ \frac{\rho u_i}{r} \right] n_i dS \propto \left( \frac{U_o}{D} \right) \left( \frac{\rho_o U_o}{r} \right) (D^2) \propto \frac{U_o^2}{r}. \quad (1.16)$$

This analysis assumes that the freestream Mach number is much less than unity or  $M = \frac{U_o}{c_o} \ll 1$ , and that far-field acoustic radiation dominates the signal so that it acts as a spherically-spreading pressure wave.

Furthermore, the radiated acoustic power  $W$ , is proportional to the square of the pressure field, giving

$$I : W \propto p'^2 \propto \frac{U_o^8}{r^2}, \quad (1.17)$$

$$II : W \propto p'^2 \propto \frac{U_o^6}{r^2}, \quad (1.18)$$

$$III : W \propto p'^2 \propto \frac{U_o^4}{r^2}. \quad (1.19)$$

The results of the scaling analysis presented in equation 1.17 correspond physically to the radiation pattern of a volumetric distribution of quadrupole sources. Therefore, Lighthill's acoustic analogy states that the far-field acoustic pressure field of a region of turbulence in a steady flow, and a region of quadrupole acoustic sources with no flow, are equivalent. Similarly, equations 1.18 and 1.19 represent a distribution of dipole and monopole sources, respectively. Finally, this analysis shows that a decrease in acoustic power of the system corresponds to an increase in acoustic efficiency when transitioning from a quadrupole to a dipole to a monopole source. These trends are extremely useful in determining the nature of the acoustic sources present in flows around complex geometries, such as aircraft landing gears.

### 1.3 Landing Gear

As previously stated, aircraft landing gear have been identified as a primary source of airframe noise especially for the larger wide-body configurations. Landing gear generally come in two types: nose landing gear (NLG) and main landing gear (MLG). The former is designed for steering while the latter is designed for braking. The scope of this study is limited to work on the G550 nose landing gear, but while designs are aircraft-specific, it is probable that flow control strategies will be derived from general flow behavior, and therefore be universally applicable.



Figure 1.1. Photograph of Gulfstream 550 Nose Landing Gear.

### 1.3.1 Geometry

The Gulfstream G550 Nose landing gear was selected due to an industry collaboration with NASA. In Neuhart et al., this design was aerodynamically characterized to provide a database of aerodynamic and acoustic data by which to compare experiments and simulations [19]. The actual landing gear is depicted in Figure 1.1 for reference, and shown schematically in Figure 1.2.

### 1.3.2 Noise Sources

Recall that adding a solid boundary to the flow drastically altered the source terms in equation 1.10. In experiments, these terms manifest as flow-generated noise, of which there are two types: 1) Tonal which is generated by periodic flow events, such as vortex shedding, and 2) Broadband which is generated by random flow events, like

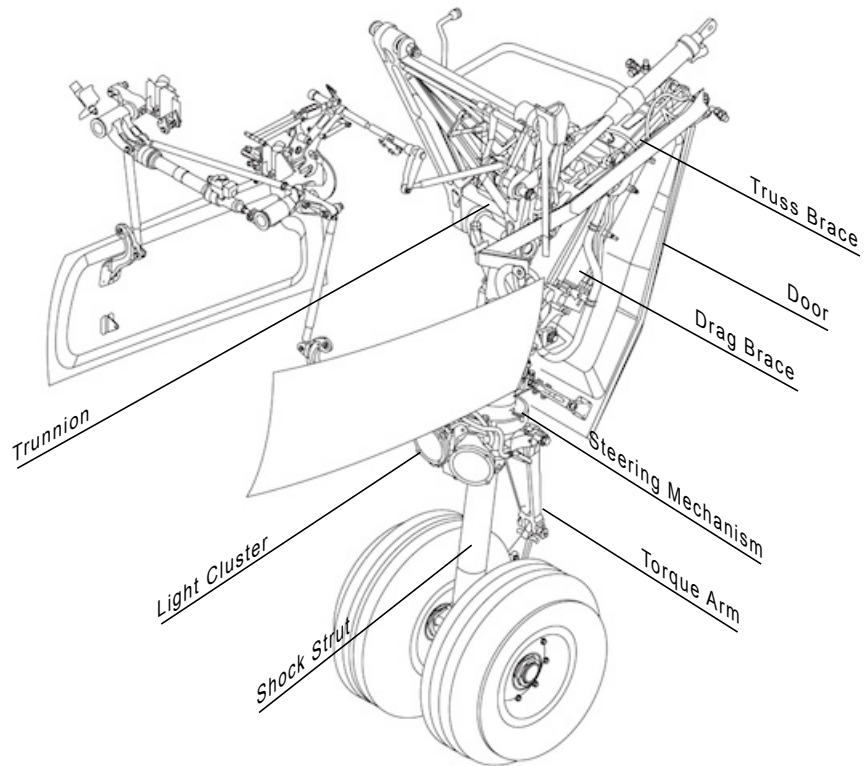


Figure 1.2. Schematic view of Gulfstream 550 Nose Landing Gear components [9].

those present in turbulence.

To develop technology to control these flow events, it is useful to understand the structures that cause them. Most aerodynamic bodies are characterized by their drag force, where the total drag force is made up of viscous drag and pressure drag components. When a body is streamlined, it is said that the total drag force is dominated by the viscous forces; while bodies characterized by a large pressure drag force, are referred to as bluff. Bluff bodies can be a major contributor to flow-generated noise, due in part to the unsteady wake these structures tend to cause.

The canonical example of a bluff body is a simple cylinder, for which the flow is well understood. It is dominated by large-scale vortex shedding of frequency  $f$ , over the cylinder body of characteristic length  $L$ . This vortex shedding frequency is characterized by the dimensionless Strouhal number  $St = \frac{fL}{U_o}$  where  $U_o$  is the freestream velocity. This large-scale vortex shedding corresponds to periodic unsteady surface pressure which is responsible for the generation of tonal noise.

More complex geometries such as aircraft landing gear, can be considered as a collections of bluff bodies. As depicted in Figure 1.1, the landing gear components are arranged in close proximity to one another. However unlike the single cylinder, tonal behavior is not observed. The acoustic signature for the landing gear is broad-band in nature which is associated with turbulence [23].It is possible that the close proximity of gear components inhibits full wake development, effectively preventing the development of large-scale vortex shedding. This suggests that flow control on simplified geometries, while academically interesting, may not be representative of the flow physics present in actual aircraft structures. This is the foundation for the suggested strategy of examining sub-systems, proposed in Chapter 3.

In addition to varying inter-component spacings, the presence of multiple length scales in the landing gear geometry implies that some components may also contribute to the total noise as reflective sources. Guo et al., measured far-field noise propaga-

tion for full-scale Boeing 737 main landing gear and classified it into regimes based on the concept of acoustic compactness [10]. Since an acoustic wave in a medium is governed by the speed of sound then  $c_o = \lambda f$ , a source is said to be acoustically compact if  $kL \ll 1$  where  $k$  is the acoustic wavenumber defined as  $k = \frac{2\pi}{\lambda} = \frac{2\pi f}{c_o}$ ,  $\lambda$  is the acoustic wavelength, and  $L$  is the characteristic length. It is noncompact if  $kL \geq 1$ . In Guo et al., large (wheels and doors) and medium geometries (main struts and linkages) represented low and mid-range frequency, acoustically compact sources, respectively; while small geometries (hoses, sharp edges, and electrical wiring) represented high frequency, noncompact acoustic sources. This is significant because compact sources behave like a distribution of dipoles, whereas noncompact sources tend to emit as, less efficient, quadrupoles.

Before discussing a strategy for flow control, it is useful to first consider the physical phenomena present. While quantifying the contribution of each mechanism to the total acoustic signature of the landing gear, is a fairly difficult task, an order-of-magnitude analysis can be applied to estimate a potential dominant source. Table 1.1 lists the mechanisms considered, acoustic power, noise type, and source type. Recall that high acoustic power corresponds to low acoustic efficiency, meaning a monopole source is a more effective noise producer than a quadrupole source. Focusing on the more efficient dipole sources present, the mechanisms of unsteady wake and downstream wake impingement are the most viable candidates for flow control. Note that vortex shedding may be present but is highly tonal, and the broadband nature of landing gear noise suggests that this is probably a minor noise producer. These physical phenomena are considered in the following review of literature.

TABLE 1.1

Physical mechanisms of flow-generated noise.

Mechanism	Acoustic Power	Source Type	Noise Type
Vortex Shedding	$\frac{U_o^6}{r^2}$	Dipole	Tonal
Wake Shear Layer	$\frac{U_o^8}{r^2}$	Quadrupole	Broadband
Wake Turbulence	$\frac{U_o^8}{r^2}$	Quadrupole	Broadband
Downstream Wake Impingement	$\frac{U_o^6}{r^2}$	Dipole	Broadband
Unsteady Wake	$\frac{U_o^6}{r^2}$	Dipole	Broadband
Reflective Sources	$\frac{U_o^8}{r^2}$	Quadrupole	Tonal or Broadband

## 1.4 Literature Review

This section provides a review of aeroacoustic research pertinent to the development of the aforementioned plasma fairing technology.

### 1.4.1 Single Cylinder Plasma Flow Control

The single cylinder is the most simplified representation of the landing gear main strut. Active flow control efforts by means of DBD plasma actuators were first applied to this generic bluff body geometry as proof-of-concept. Several experiments and large-eddy simulations (LES) were performed at the University of Notre Dame to show the viability of this technology [15] [16]. Two flow control technologies were employed: spanwise plasma actuators, and plasma streamwise vortex generators (PSVGs). The former of these devices consists of spanwise-oriented, exposed electrodes fixed about the geometry's separation points, while the latter is made up of a spanwise array of electrodes oriented in the streamwise direction. The construction and accompanying electronic circuit of these actuators are well documented in

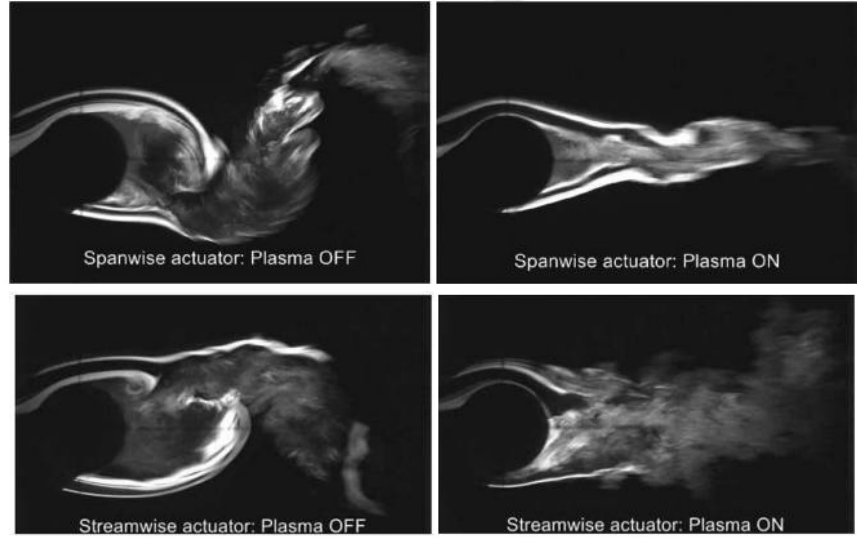


Figure 1.3. Flow Visualization of single cylinder in cross-flow with Spanwise and PSVG plasma actuators.

Kozlov et al. [16]. Flow visualization demonstrating the effects of these devices is shown in Figure 2.12.

Both approaches were effective in significantly suppressing large-scale vortex shedding, if by different mechanisms. Spanwise plasma actuators achieve flow control through modification of the detached free shear layer. PSVGs induce streamwise vorticity into the nascent cylinder wake, promoting rapid wake mixing. Kozlov et al. performed near field microphone measurements at  $d = 0.61$  m, demonstrating a reduction in noise levels of 11.2 dB and 14.2 dB for spanwise actuators and PSVGs, respectively [16]. These results were promising and inspired more studies on a slightly more complex geometry: tandem cylinders.

#### 1.4.2 Tandem Cylinders Plasma Flow Control

The tandem cylinders configuration is the next stage in the development of active plasma flow control for aircraft landing gear. Similar to the work on the single cylinder, experiments and LES were also performed for tandem cylinders as reported

in [6] [14] [17]. The interaction between the two bluff bodies represents that between the main strut and downstream components of an aircraft landing gear. In 1985, Zdravkovich comprehensively reviewed two circular cylinders of the same diameter at subcritical Reynolds number [24]. In this study, tandem cylinder flow is classified into regimes based on the ratio  $L/D$  where  $L$  is the center-to-center length between the cylinders and  $D$  is the cylinder diameter. Using the results of this study, Kozlov et al. examined the wake interaction of tandem cylinders in the intermittent shedding regime [17]. Both spanwise actuators and PSVGs were applied to the upstream cylinder, and were successful in reducing  $Cp_{rms}$  by 65% and 47%, respectively. This was accomplished by reducing the extent of large-scale vortex shedding in the upstream cylinder wake as shown in Figure 1.5. While the acoustic effects of this were not documented experimentally, simulations demonstrated the reduction of peak sound pressure level by approximately 16 dB, confirming the viability of plasma actuation for active aeroacoustic control of airframe noise [6].

#### 1.4.3 Shock Strut-Torque Arm Assembly Plasma Flow Control

Studies performed by Neuhart et al., identified the torque arm as a region of high noise production on aircraft landing gear. Huang et al. studied the acoustic effects of plasma actuators on a torque arm apparatus [13]. By applying spanwise plasma actuators in both 'upstream' and 'downstream' configurations, two types of flow control were explored. The upstream configuration served to create a virtual plasma fairing effect by routing the shear layers around the downstream components, reducing the overall noise generated by wake impingement. The downstream configuration is shown to have reduced vortical structures, lowering the unsteadiness in the wake. The downstream and upstream configurations reduced far-field noise by 1.7 and 3.1 dB, respectively [13]. Wicks et al. also studied this geometry [22]. The spanwise actuation strategy was utilized and flow visualization is given in Figure 1.5.

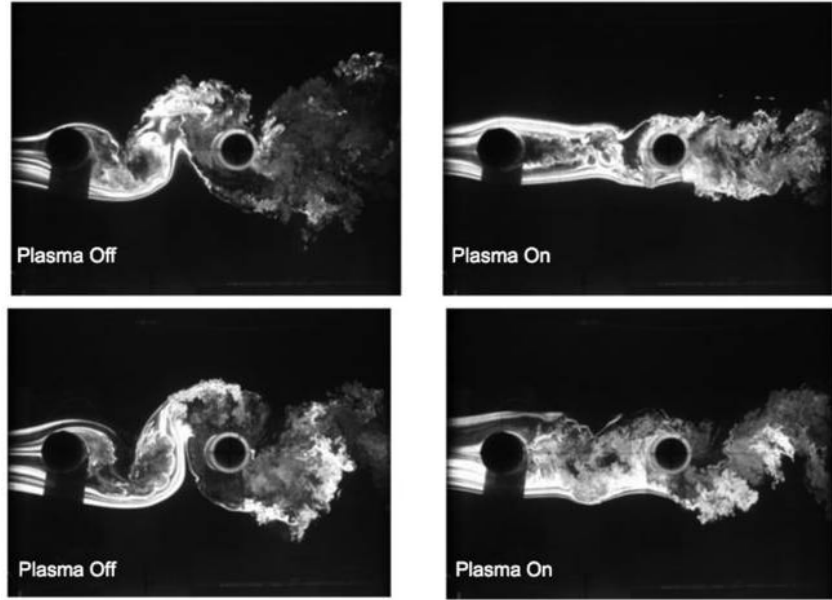


Figure 1.4. Flow Visualization of tandem cylinders in cross-flow with Spanwise and PSVG plasma actuators.

While this study did not focus on acoustic measurements, surface pressure spectra revealed a significant reduction in unsteady surface pressure associated with the wake of the upstream cylinder. Unfortunately, this had the adverse effect of increasing the energy of the wake of the downstream cylinder, demonstrating a fundamental difference between this geometry and the tandem cylinders. It also suggests perhaps a flow control strategy emphasizing the reduction of the extent of the wake impingement as opposed to large-scale vortex shedding may prove more successful in noise reduction.

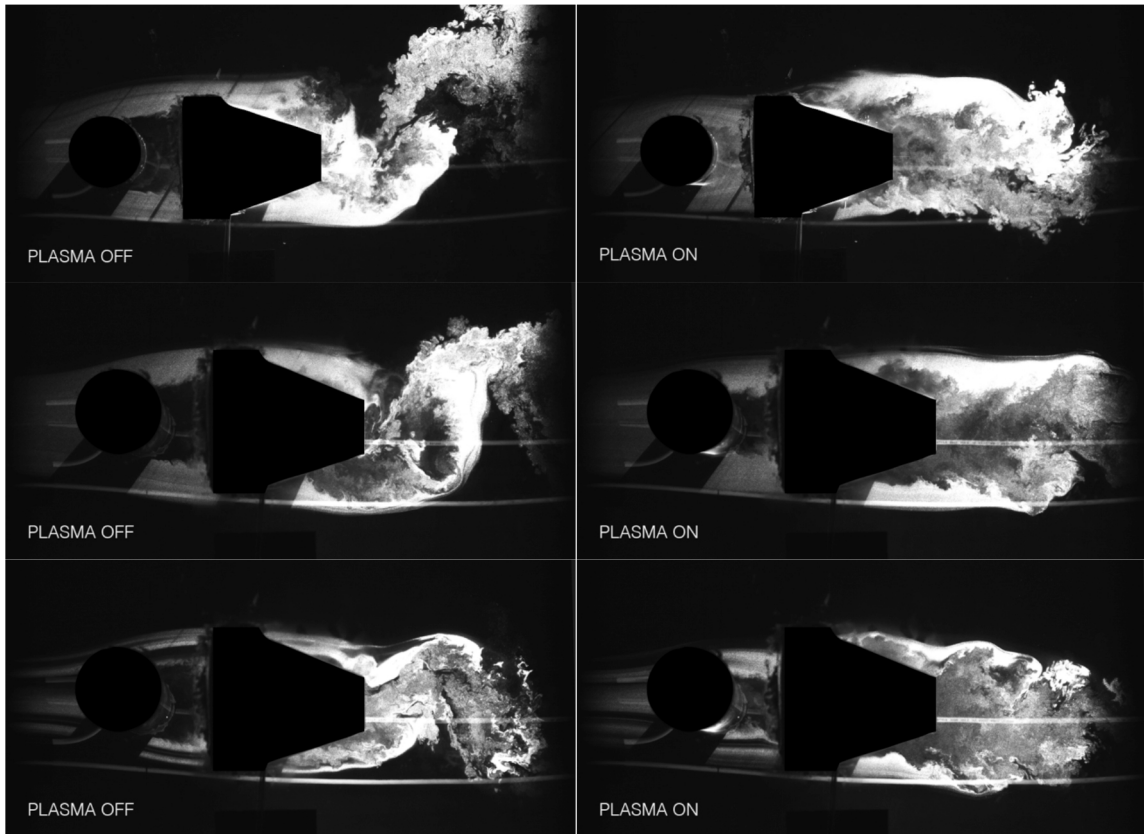


Figure 1.5. Flow Visualization of torque-arm assembly in cross-flow with Spanwise plasma actuators.

## CHAPTER 2

### EXPERIMENTAL APPROACH

The following chapter provides details on the experiments completed to date

#### 2.1 Experimental Objective

Several key features of the flow over aircraft landing gear geometry have yet to be fully understood. One such feature is the main strut and door interaction. The preliminary experiments outlined in this chapter, exploring this interaction, have revealed potentially viable flow control strategies to be investigated in the proposed experiments outlined in chapter 3.

#### 2.2 Experimental Facility

Acoustic measurements were obtained in the Notre Dame Anechoic Wind Tunnel Facility (ND AWT). The ND AWT is a low-noise, open-jet acoustic wind tunnel with a free jet test section measuring 24-in-(0.610 m)-high by 24-in-(0.610 m)-wide installed in a large anechoic chamber suitable for frequencies above 100 Hz. The maximum empty test section velocity is approximately  $U_\infty = 35$  m/s. The maximum safe tunnel velocity with the Notre Dame G550 Nose Landing Gear 30%-scale model (ND G550) installed is 30 m/s corresponding to a Mach number of  $M_\infty = 0.1$ .

Atmospheric properties such as ambient temperature and pressure were acquired using a digital thermometer and barometer. The tunnel speed is measured using a pitot-static probe installed approximately 6 in (0.154 m) from the free jet inlet centerline. From these data local sonic speed and the flow Mach number are computed.



(a) Baseline 1



(b) Baseline 2

Figure 2.1. ND G550 model with and without plasma fairing installed.

### 2.3 Notre Dame G550 Nose Landing Gear Model

The Notre Dame G550 (ND G550) nose landing gear model has two baseline configurations without plasma actuation. The first, designated Baseline 1, consisted of the ND G550 model without the plasma fairing installed, which is shown in the photograph of Figure 2.1a. The second, designated Baseline 2, involved the ND G550 model retrofitted with a plasma fairing assembly in order to facilitate the installation of DBD plasma actuators for flow control. This configuration is shown in the photograph of Figure 2.1b.

Spanwise plasma actuators were fixed to the  $\pm 90^\circ$  locations to ascertain the effects on the flow. The plasma actuator was constructed using 1/8 in ULTEM dielectric and 1 in exposed and covered copper electrodes. Also, it was operated using a sine wave carrier frequency of 1 kHz with 40 kV peak-to-peak voltage. With this configuration, the plasma actuators can be operated in both two-sided and one-sided modes.

### 2.4 Microphone Measurements

A polar array of omnidirectional microphones was used to acquire far field noise level spectra along the length of the AWT test section. It consists of a 1/2-in ACO Model 7046 electret microphone with companion 4012 preamplifier and PS9200 power supply. A schematic illustrating the array is shown in Figure 2.2. Additionally, the array configuration relative to the G550 model is shown in the photograph of Figure 2.3. The microphone is mounted using a microphone stand so as to protrude from an acoustically treated rail by approximately 13 in (0.330 m). The total range of acoustic source-to-microphone angle spanned by the polar array is approximately  $30^\circ \leq \theta \leq 150^\circ$  as referenced from the upper torque arm of the model in the downstream flow direction. As shown in Figure 2.3, the polar array is situated along the length of the free jet test section and positioned at the same height as the upper torque arm of the

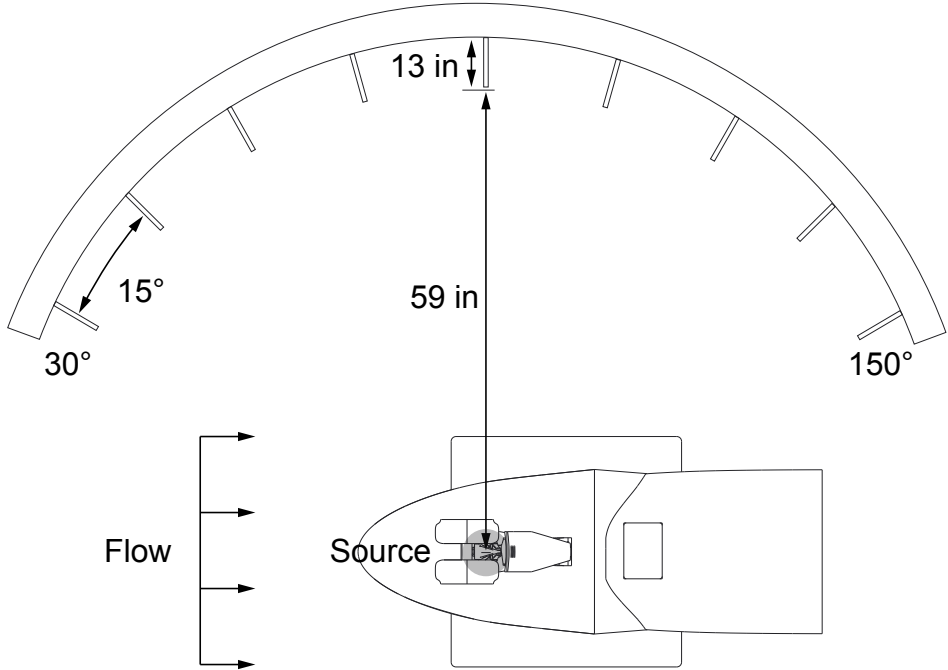


Figure 2.2. Schematic of the polar array.

model, with the plane of the microphone located approximately 59 in (1.50 m) from the test section centerline.

## 2.5 Flow Visualization

A commercial time-resolved PIV system comprising a Litron Nd:YLF ( $\lambda = 527$  nm) dual-cavity laser and Photron SA1 high-speed camera (12 bit, maximum resolution  $1280 \times 800$  pixels) was utilized. This system was operated in single-frame mode at a repetition rate of 2k frames per second (fps). Images were acquired with a spatial resolution of  $1020 \times 1020$  pixels. During each run,  $N = 2k$  images were recorded. A 60 mm Nikon Nikkor Micro lens was fitted and oriented orthogonal and  $45^\circ$  to the flow (to resolve region between main strut and door). The experimental setup is depicted in Figure 2.4.

Continuous DEHS fog consisting of nominally 1-mm-diameter droplets generated

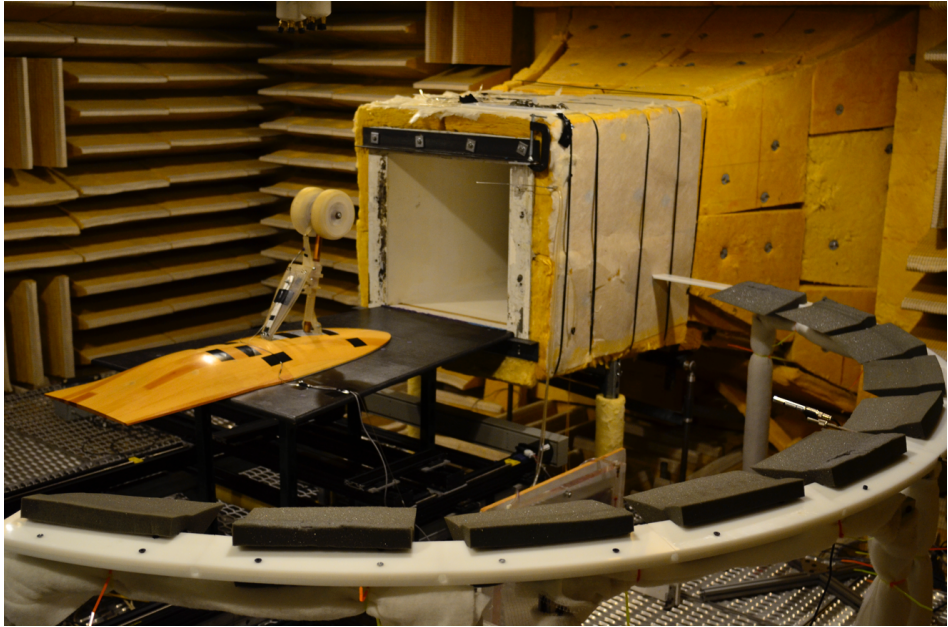


Figure 2.3. Photograph of the polar array installed in the ND AWT.

by a TSI six-jet particle atomizer were introduced upstream of the wind-tunnel inlet contraction. The Nd:YLF laser was used to illuminate the fog in a spanwise plane located 6 in from the base of the model. Flow visualization was performed with baseline 1, 2, and plasma on, in order to assess the global influence on the wake interaction with the main strut and door.

## 2.6 Data Acquisition

For microphone data acquisition, a National Instruments USB-6343 DAQ was used, yielding a total of 45 available channels with 48-bit ADC. The sampling parameters for the microphone data acquisition are listed in Table 2.1.



Figure 2.4. Photograph of the experimental setup for high speed flow visualization.

TABLE 2.1

Data acquisition parameters.

Sensors	Sampling Rate (Hz)	$\frac{Samples}{block}$	Window Function	Overlap (%)	$N_{blocks}$	$N_{averages}$	Acquisition Time (s)
ACO	65,536	2048	Hanning	0	960	960	30

## 2.7 Current Results

### 2.7.1 Wind Tunnel Background Noise Characterization

It was deemed important to establish that the background noise levels in the ND AWT were sufficiently below that of the ND G550 model. To that end, measurement of noise levels for both Baseline 1 and Baseline 2 G550 configurations were compared with those obtained with the AWT tunnel running empty. Figure 2.5 presents a representative comparison of 1/3-octave band sound pressure level (SPL) spectra obtained for the Baseline 1 configurations and the empty tunnel. The figure clearly shows that the background empty tunnel noise level is several orders of magnitude below that of the ND G550, so that the effects of plasma flow control on noise production will be detectable in this facility.

### 2.7.2 Far field check

This section describes a procedure for verifying the far field assumption for microphone measurements. For a microphone measurement to be classified as far field, the microphone-to-source distance must be greater than the acoustic wavelength. To check this, a relation can be made between power spectral density,  $PSD$ , and microphone-to-source distance,  $d$ . Recall from equation 1.9 that  $p' \propto 1/d$ , therefore, it follows that  $PSD \propto 1/d$ . Combining this relation at  $d = 48$  in and  $d = 59$  yields,

$$\frac{PSD_1}{PSD_2} \propto \frac{d_2}{d_1} \propto 1.23. \quad (2.1)$$

The  $PSDs$  at both of these locations is plotted along with a reference line at 1.23 in Figure 2.6. The measured microphone data exhibits oscillations about the theoretical value of 1.23. Also, the average of the oscillations collapses to approximately this value if frequencies below 100 Hz are excluded. This suggests that to resolve frequencies below 100 Hz larger values for  $d$  are necessary. Previous experiments on

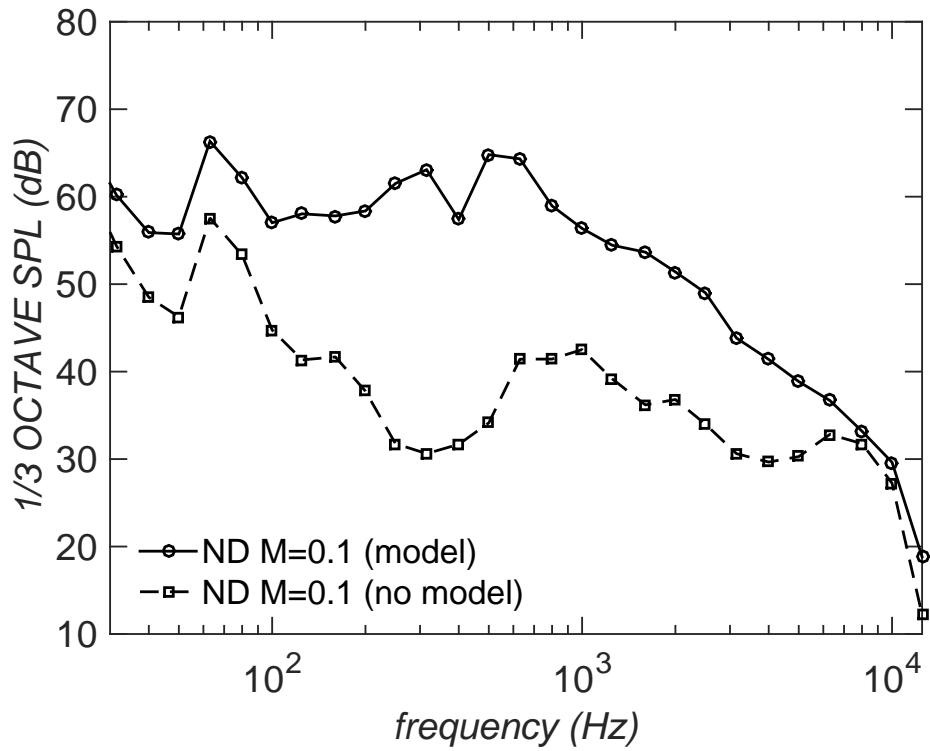


Figure 2.5. Representative far field noise level with and without Baseline 1 model installed at  $\theta = 90^\circ$

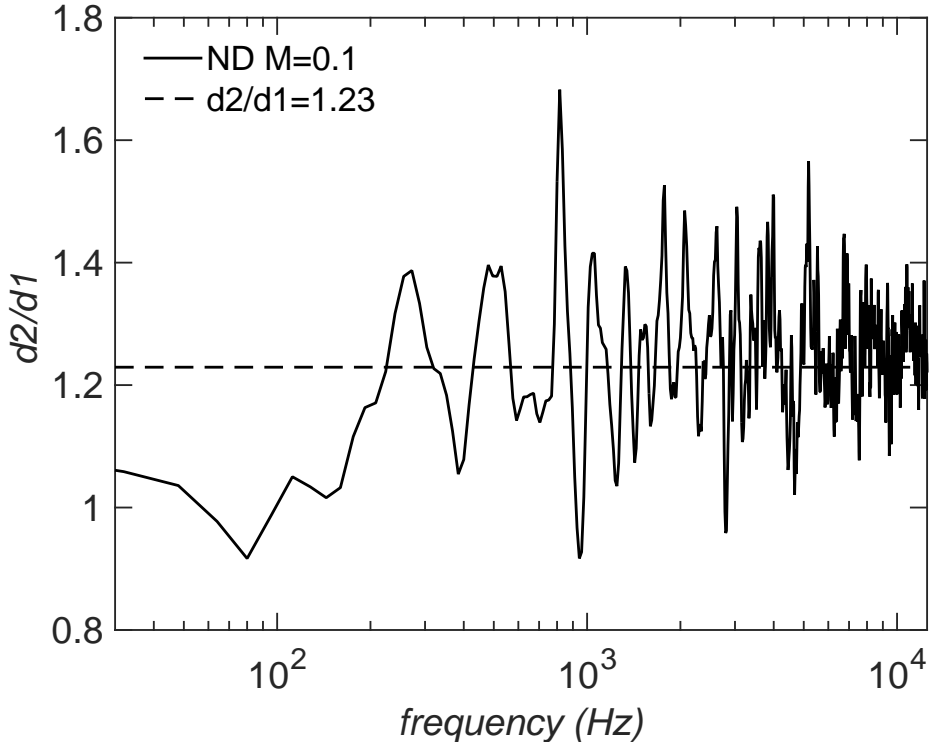


Figure 2.6. Far field measurement analysis for  $d = 48$  in and  $d = 59$  in at  $\theta = 90^\circ$

landing gear geometry have reinforced that this lower limit on acoustic measurements is acceptable, as most observed flow behavior is attributed to frequencies above this cutoff.

### 2.7.3 Comparison with UFAFF Measurements

In this study, the far field microphone distance  $d$ , was 72 in (1.83 m) array-to-model and 59 in (1.50 m) microphone-to-model. However, previous studies conducted at the University of Florida Anechoic Flow Facility (UFAFF) on the NASA G550 model were performed at a source-to-microphone distance of 48 in. In order to form a basis for comparison with acoustic results from that study, 1/3-octave band SPL spectra were obtained with the ND Baseline 1 model in the ND AWT

for a source-to-microphone distance of 48 in (1.22 m). Even after accounting for the source-to-microphone distance disparity, the UFAFF experiments were performed at a freestream Mach number  $M_\infty = 0.189$  and the Notre Dame experiments were performed at  $M_\infty = 0.1$ . The effect of disparate Mach numbers on the SPL can be accounted for by scaling the Notre Dame results via the relation,

$$SPL_2 = SPL_1 - 10 \log \left( \frac{M_1}{M_2} \right)^6, \quad (2.2)$$

where  $SPL_1$  and  $M_1$  denote the ND AWT experimental values,  $M_2$  denotes the UFAFF test Mach number (0.189) and  $SPL_2$  represents the ND AWT sound pressure level values corrected for Mach number. Figure 2.7 compares 1/3-octave band SPL spectra obtained in both facilities for the case of  $\theta = 90^\circ$ . In this plot the frequency is expressed in terms of Strouhal number,  $St_D = fD/U_\infty$ , where length scale  $D$  is the shock strut diameter upstream of the torque arm and  $U_\infty$  is the freestream velocity. There is good collapse of the NASA G550 and ND G550 data from  $0.3 \leq St_D \leq 0.6$ . Below this range there is about 4-5 dB difference before the 100 Hz AWT cutoff frequency. Above this range there is significant discrepancy. The NASA G550 model is characterized by a peak near  $St_D = 3$  and spectral roll-off above this peak. The ND G550 model lacks this high frequency content. The components of the ND G550 model are mostly fabricated from SLA plastic, while the NASA G550 consists of mostly aluminum and carbon fiber. To compensate for the differences in tensile strength, thickness was added to several components of the ND G550 model as shown in the CAD images in Figure 2.8. Additionally, it was necessary to construct most of the ND G550 model from plastic to facilitate the retrofitting of plasma actuators. It is possible, but by no means certain that these design modifications may play a role in the observed differences in noise spectra.

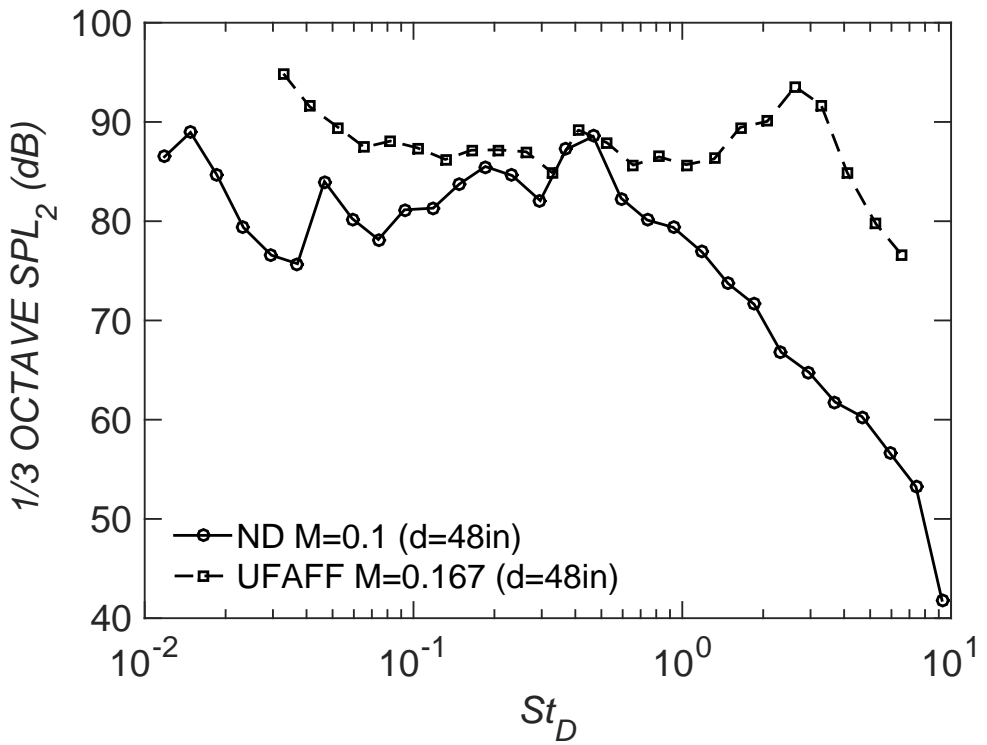


Figure 2.7. Comparison of far field noise level at UFAFF and ND AWT facilities at  $\theta = 90^\circ$

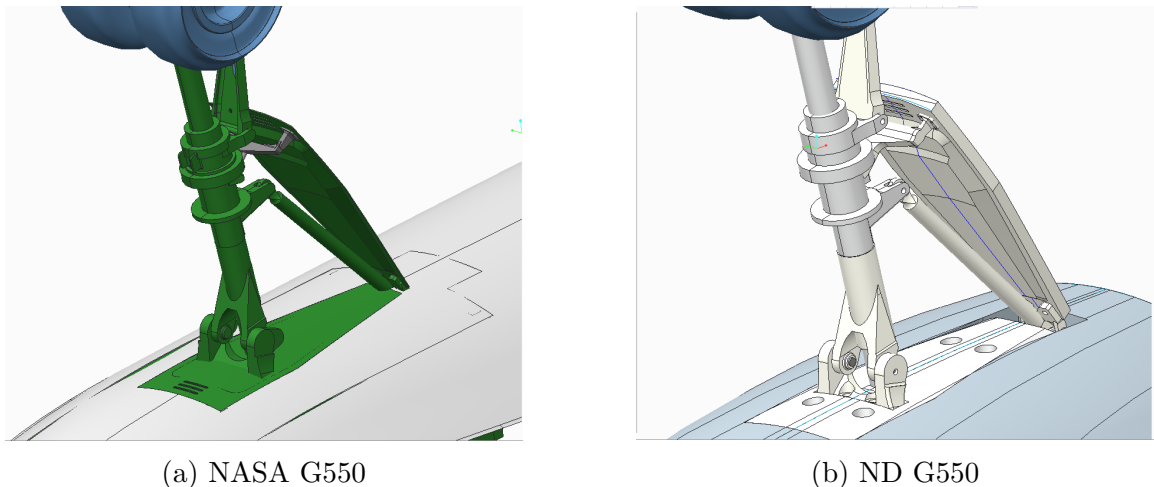


Figure 2.8. Comparison of design of the NASA G550 and ND G550 model geometries.

#### 2.7.4 Effects of Tripping

Previous work on the NASA G550 Nose Landing Gear (NASA G550) involved application of serrated transition strips that were applied along the length of the shock strut in order to create a turbulent boundary layer prior to separation. For consistency with this previous work, the influence of similar aerodynamic trips was explored on the ND G550 Baseline 1 model. A distributed roughness element made of standard diving board tape was fixed to the shock strut. Sample results comparing 1/3-octave band SPL spectra for the tripped and untripped cases are presented in Figure 2.9. This figure shows that there was very little influence of the trip on radiated noise. Since a trip would restrict the optimum placement of the plasma actuators, it was omitted from the model and the acoustic results that follow were obtained without tripping unless otherwise indicated.

#### 2.7.5 Preliminary Acoustic Assesment

Three key locations on the polar array were selected for microphone measurements. This allowed several plasma actuator configurations to be tested expediently to quickly assess noise reduction. Four plasma actuator configurations were utilized: 1) Baseline 1, 2) Baseline 2, 3) Sine 40 kV (Two-sides), 4) Sine 40 kV (One-side). The effect of the fairing geometry is shown with 1) and 2), while 3) and 4) demonstrate the effects of plasma actuation. The maximum peak-to-peak voltage attainable with the ULTEM dielectric was 40 kV before signs of dielectric failure were observed. In subsequent experiments, a dielectric that is less susceptible to failure, such as quartz, is recommended.

The 1/3-octave band SPL spectra for the aforementioned actuator configurations are given in Figure 2.10. Recall from Figure 2.5, that the left most peak is below the 100 Hz cutoff frequency and is most likely due to fan noise inherent to the facility. The acoustic signature at each location is characterized by two peaks at approximately

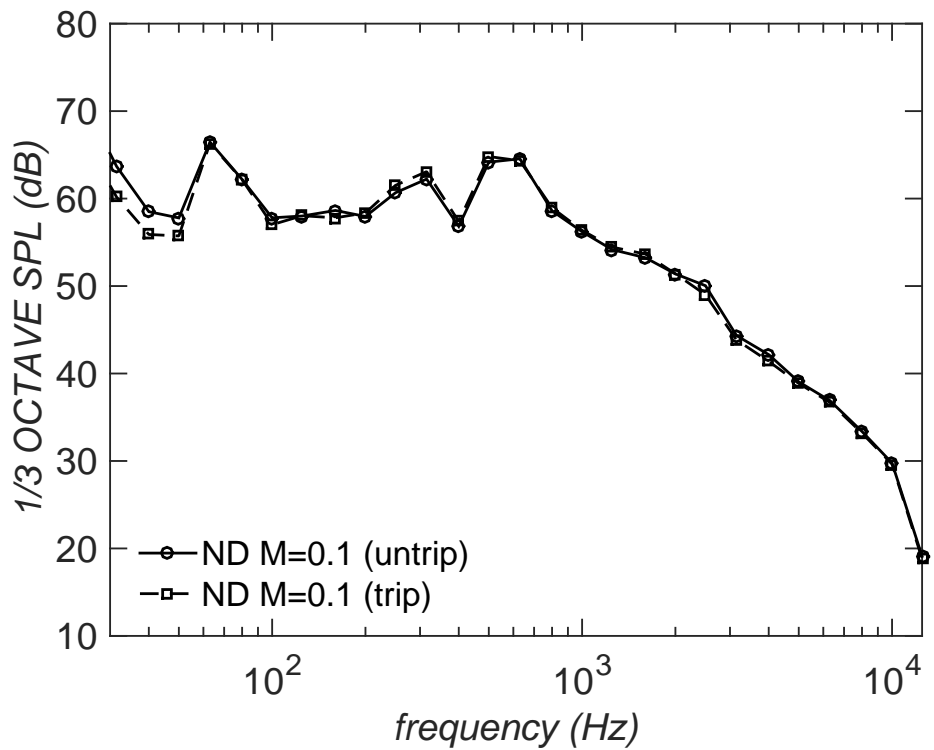


Figure 2.9. Comparison of far field noise level with and without the presence of a trip at  $\theta = 90^\circ$

300 Hz and 500 Hz of varying magnitude. Most of the change caused by the plasma fairing occurs around these frequencies, with the exception of a slight increase in frequency due to the self-noise of the plasma actuators for  $6 \leq f \leq 12.5$ .

The Overall Sound Pressure Level (OASPL) is calculated by integrating the power spectral density from  $100 \leq f \leq 1000$  Hz. This range was selected to eliminate any effects from the self-noise generated by the plasma actuator which is operated at a carrier frequency of 1000 Hz. OASPL at each location,  $\theta = 45^\circ, 90^\circ, 135^\circ$ , is given in Figure 2.11. There is a slight decrease for the Baseline 2 and sine 40 kV one-side cases at  $\theta = 135^\circ$  of 0.12 dB and 0.13 dB, respectively. Also, the plasma actuation actually increased the noise at each location with the exception of the sine 40 kV one-sided case at  $\theta = 135^\circ$ .

To better understand the perplexing results of the acoustic measurements, flow visualization was performed to resolve the change to the global flow field and the effects on the main strut and door wake interaction. These images are given in Figure 2.12. When comparing the global flow field of Baseline 1 and 2, it is clear that the addition of the fairing acts to increase the spanwise extent of the wake caused by the upstream main strut. This results in reduction of the impingement of the detached shear layers on the downstream door. Interestingly, the activation of the plasma actuators in both two-sided and one-sided modes created a global flow field closer to that of the Baseline 1 case. Also, the plasma actuators increased unsteadiness in region between the the main strut and door, resulting in a significant increase in noise.

While these initial results show an increase in noise due to plasma actuation, there are implications for favorable flow control strategies. Configurations of plasma actuators that direct the detached shear layers around landing gear components may result in a significant reduction in noise. This could be accomplished by using spanwise plasma actuators to ‘trip’ the flow, causing premature flow separation on the

plasma fairing. Additionally, wake unsteadiness could be accomplished by utilizing PSVGs to promote mixing, thereby reducing large-scale vortices in size.

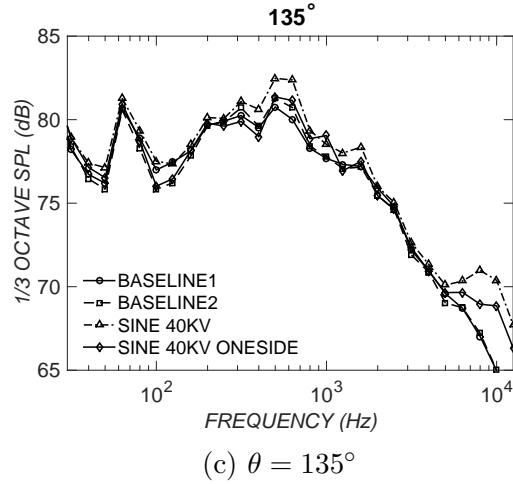
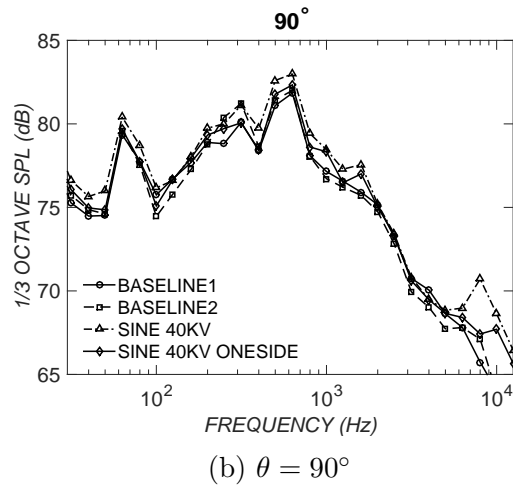
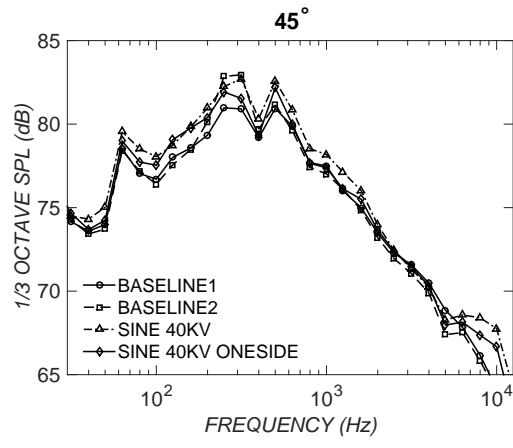


Figure 2.10. 1/3-octave band sound pressure level for various plasma actuator configurations.

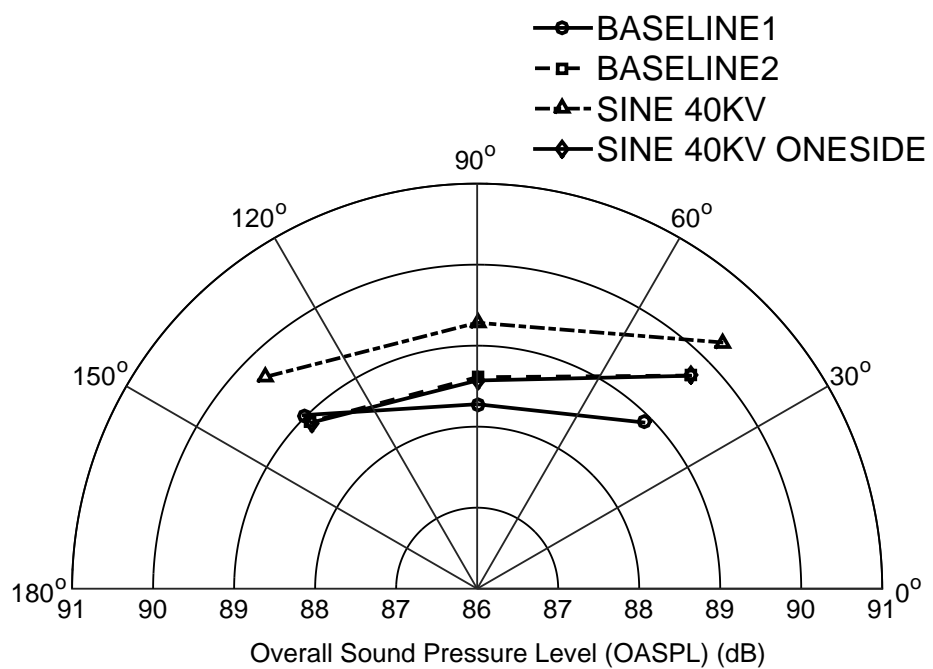


Figure 2.11. Overall sound pressure level at key polar array locations.



Figure 2.12. Landing gear flow visualization orthogonal (left) and at  $45^\circ$  (right).

## CHAPTER 3

### OBJECTIVES AND FUTURE WORK

This chapter outlines the research objectives and proposed future work.

#### 3.1 Research Objectives

The overall focus of this study is the development of plasma fairing technology, however, much has yet to be accomplished before this technology is flight ready. To this end, the complex ND G550 geometry will be divided into two sub-systems: 1) main-strut-door assembly and 2) the shock-strut-torque-arm assembly. Flow control strategies will be explored for each of these subsystems varying plasma actuator configurations. Finally, the acoustic effects of the applied flow control will be characterized.

While the ultimate purpose of this research is the reduction of noise on aircraft landing gears, the objectives of this study will emphasize the documentation of the most successful flow control strategies and underlying physical mechanisms responsible. Regardless if noise reduction is actually achieved, there is much to be gained through a deeper understanding of the effects of various flow control strategies on noise generation.

#### 3.2 Proposed Future Work

The following sections detail the experiments that will be performed to accomplish the outlined research objectives.

### 3.2.1 Plasma Actuator Configuration

Recall from Figure 2.1b, the plasma fairing that has been retrofitted to the ND G550 nose landing gear model. Plasma actuators will be fixed to this partial fairing geometry. Both spanwise and PSVG configurations will be explored. The effects of geometric parameters will be examined such as spanwise actuator azimuthal placement and upstream versus downstream forcing. Also, the effects of plasma actuation parameters such as voltage, frequency, and interelectrode spacing (PSVGs only).

As parameters are varied the changes to the flow field will be documented using high speed flow visualization similar to that in Figure 2.12. Particle Image Velocimetry (PIV) will be performed to quantify these flow fields and calculate the effects on vorticity, as changes to vorticity can result in significant changes to the acoustic signature.

From the preliminary results cited in the previous chapter, a minor reduction in noise was observed when the main strut wake impingement was reduced on the downstream door. Unsteady pressure sensors will be used at various locations near the door's edge to quantify the effect of varying the parameter space of the plasma actuator. Both power spectral density and RMS pressure coefficient will be calculated.

### 3.2.2 Noise Reduction Assessment

The plasma actuator configurations deemed most likely to reduce noise will be selected based on the previous measurements. These configurations will then be tested on the model in the AWT facility. The polar array depicted in Figure 2.3 will be used to measure magnitude and directivity of noise generated by baseline model and with plasma actuators installed. The difference in overall sound pressure level (OASPL) will also be calculated. It is possible that iteration will be necessary to identify the most promising plasma actuator configurations, as reduction in unsteady pressure is

not necessarily indicative of noise reduction of a similar magnitude. Finally, phased-array noise source identification will be performed to reveal where on the ND G550 model, flow control was most effective. Analysis of the underlying mechanisms will also be presented, by correlating aerodynamic and acoustic data.

### 3.3 Conclusion

While preliminary experiments demonstrate only a marginal effect of plasma flow control on noise reduction, flow visualization suggests a “path forward”, by focusing on the elimination of wake impingement of the main strut on the door. Additionally, studies performed on the shock strut and torque arm geometries confirm that this flow control strategy may apply to other locations of aircraft landing gear. Several plasma actuator configurations will be utilized while documenting both the aerodynamic and acoustic effects. This study will focus on the underlying physical mechanisms responsible for noise production on the ND G550 nose landing gear model and the effects of flow control via plasma actuation.

## BIBLIOGRAPHY

1. M. A. Busquin. European aeronautics: A vision for 2020, meeting society's needs and winning global leadership. Rept. of the group of personalities, Advisory Council for Aeronautics Research in Europe, Jan 2001.
2. A. W. Correia, J. L. Peters, J. I. Levy, S. Melly, and F. Dominici. Residential exposure to aircraft noise and hospital admissions for cardiovascular diseases: multi-airport retrospective study. *BMJ*, 347, 2013.
3. N. Curle. The influence of solid boundaries upon aerodynamic sound. *Proceedings of the Royal Society A: Mathematical and Physical Sciences*, 231(1187):505–514, 1955.
4. W. Dobrzynski. Almost 40 years of airframe noise research: What did we achieve? *Journal of Aircraft*, 47(2):353–367, April 2010.
5. W. Dobrzynski, L. C. Chow, P. Guion, and D. Shiells. Research into landing gear airframe noise reduction. AIAA/Conference European Aerospace Societies Paper 2002-2409, June 2002.
6. A. Eltawee, M. Wang, D. Kim, F. O. Thomas, and A. Kozlov. Numerical investigation of tandem-cylinder noise reduction using plasma-based flow control. *J. Fluid Mech*, 756:422–451, 2014.
7. Environmental Research and Consultancy Department. Aircraft noise, sleep disturbance and health effects cap 1164. Technical report, June 2014.
8. J. S. Gibson. Non-engine aerodynamic noise investigation of a large aircraft. NASA CR-2377, 1974.
9. Gulfstream Aerospace Corporation. *G-550 Aircraft Maintenance Manual*. 2014.
10. Y. Guo, R. Stoker, and K. Yamamoto. Experimental study on aircraft landing gear noise. *Journal of Aircraft*, 43(2):306–317, 2009.
11. A. Hirschberg and S. W. Rienstra. *An introduction to aeroacoustics*. Eindhoven University of Technology, 2004.
12. M. S. Howe. *Theory of Vortex Sound - Lighthill's Theory*. Cambridge University Press, 2003.

13. X. Huang, X. Zhang, and Y. Li. Broadband flow-induced sound control using plasma actuators. *Journal of Sound and Vibration*, 329(13):2477–2489, 2010.
14. M. R. Khorrami, M. M. Choudhari, L. N. Jenkins, and C. B. McGinley. Unsteady flowfield around tandem cylinders as prototype for component interaction airframe noise. 11th AIAA/CEAS Aeroacoustics Conference AIAA Paper 2005-2866, 2005.
15. D. Kim and M. Wang. Large eddy simulations of flow over a circular cylinder with plasma based control. 47th AIAA Aerospace Sciences Meeting AIAA Paper 2009-1080, 2009.
16. A. V. Kozlov and F. O. Thomas. Bluff-body flow control via two types of dielectric barrier discharge plasma actuation. *AIAA Journal*, 49(9):1919–1931, 2011.
17. A. V. Kozlov and F. O. Thomas. Plasma flow control of cylinders in a tandem configuration. *AIAA Journal*, 49(10):2183–2193, 2011.
18. M. J. Lighthill. On sound generated aerodynamically. ii. turbulence as a source of sound. *Proceedings of the Royal Society A: Mathematical and Physical Sciences*, 222(1148):1–32, 1954.
19. D. H. Neuhart, M. R. Khorrami, and M. M. Choudhari. Aerodynamics of a gulfstream g550 nose landing gear model. 15th AIAA/CEAS Aeroacoustics Conference AIAA Paper 2009-3152, 2009.
20. H. J. Price. Faa forecast sees continued, steady growth in air travel. Website, 2015. <http://www.faa.gov>.
21. P. A. Ravetta, R. A. Burdisso, and W. F. Ng. Noise control of landing gears using elastic membrane-based fairings. AIAA/Conference European Aerospace Societies Paper 2007-3466, May 2007.
22. M. Wicks, F. O. Thomas, T. C. Corke, C. Nelson, M. Patel, and A. B. Cain. Plasma flow control on a landing gear model. 53rd AIAA Aerospace Sciences Meeting AIAA Paper 2015-1036, 2015.
23. N. S. Zawodny, F. Liu, T. Yardibi, L. Cattafesta, D. H. Neuhart, and T. Van de Ven. A comparative study of a 1/4-scale gulfstream aircraft nose gear model. 15th AIAA/CEAS Aeroacoustics Conference AIAA Paper 2009-3153, 2009.
24. M. M. Zdravkovich. Flow induced oscillations of two interfering circular cylinders. *Journal of Sound and Vibration*, 101(4):511–521, 1985.

# Mechanism of Vorticity Generation in Plasma Streamwise Vortex Generators

Michael Wicks,\* Flint O. Thomas,<sup>†</sup> and Thomas C. Corke<sup>‡</sup>

*University of Notre Dame, Notre Dame, Indiana 46556*

and

Mehul Patel<sup>§</sup> and Alan B. Cain<sup>§</sup>

*Innovative Technology Applications Company, LLC, Chesterfield, Missouri 63017*

DOI: 10.2514/1.J053997

An experimental investigation into the mechanism of streamwise vorticity generation in an array of plasma streamwise vortex generators is presented. The array is flush mounted to a flat plate on which a nominally zero pressure gradient turbulent boundary layer develops upstream. The investigation is focused on characterization of the influence of freestream velocity, applied peak-to-peak voltage, length of the active electrode, and spanwise interelectrode spacing on streamwise vorticity generation. It is shown that the actuator creates wall-normal vorticity and reorients it into the streamwise direction. In addition, spanwise boundary-layer vorticity is reoriented into the streamwise direction. Scaling relations based on the vorticity transport equation are obtained and experimentally validated. These provide guidance for optimizing the actuators for particular flow control applications.

## Nomenclature

$A_v$	=	vortex cross-sectional area in the $y-z$ plane
$E$	=	electric field
$E_{pp}$	=	peak-to-peak excitation voltage
$F_B$	=	body force vector
$L$	=	active surface electrode length
$M_\infty$	=	freestream Mach number
$Re_x$	=	Reynolds number
$\bar{S}_{xj}$	=	mean strain rate
$s_{xj}$	=	fluctuating strain rate
$U$	=	streamwise mean velocity component
$\langle \bar{U} \rangle$	=	spanwise cycle-average mean velocity
$U_\infty$	=	freestream velocity
$u_j$	=	$j$ component velocity fluctuation
$u_\tau$	=	wall friction velocity
$\bar{V}$	=	wall-normal mean velocity component
$V_p$	=	plasma-induced wall-normal velocity
$\bar{W}$	=	spanwise mean velocity component
$\bar{W}_p$	=	plasma-induced spanwise mean velocity
$x, y, z$	=	streamwise, wall-normal, and spanwise spatial coordinates, respectively
$\delta$	=	99% boundary-layer thickness
$\delta^*$	=	boundary-layer displacement thickness
$\lambda$	=	spanwise interelectrode spacing
$\Gamma(x)$	=	circulation
$\bar{\omega}_x$	=	streamwise component mean vorticity
$\omega'_x$	=	streamwise vorticity fluctuation

## I. Introduction

PASSIVE vortex generators (VGs) are widely used for separation control on both commercial and military aircraft. There are a wide variety of passive vane-type, surface-mounted VGs as reviewed by Lin [1] and Bushnell [2]. These often have vane heights on the order of the local boundary-layer thickness  $\delta$  or smaller. Some designs create pairs of counter-rotating streamwise vortices, whereas others produce corotating vortices. Regardless of the details of their design, the production of near-wall streamwise vortices that persist over a significant downstream distance promotes cross-stream momentum transfer within the boundary layer. This serves to transport relatively high-momentum fluid from the outer region toward the wall and, consequently, the boundary layer is better able to withstand an imposed adverse pressure gradient without undergoing separation. Passive VGs have several advantages for flow control applications. They are simple, robust, proven devices that are easily retrofitted to the airframe. Their major detractor is a significant drag penalty incurred in portions of the flight envelope where they are not needed. For example, Martin et al. [3] showed that the combination of a transonic leading-edge glove (which lowered the local Mach number) and passive vortex generators was extremely effective at suppressing dynamic stall on a pitching airfoil. However, the effectiveness of the transonic glove and passive vortex generator combination diminished at higher Mach numbers above  $M_\infty = 0.3\text{--}0.4$  as a result of shocks generated by the passive vortex generator. This suggests that passive VGs may give rise to a shock-induced drag penalty on the advancing rotor. In fact, there are many applications in which it is desirable to generate streamwise vorticity when boundary-layer separation is a possibility and have the VG effectively disappear when not needed. This is the basis of the plasma streamwise vortex generator (PSVG) actuators that are the focus of this paper.

The PSVG actuators are flush, surface-mounted active flow control actuators that are designed to use the body force vector field associated with dielectric barrier discharge (DBD) plasma actuation to create streamwise vorticity in a manner similar to passive VGs. Readers unfamiliar with application of DBD plasma actuators for aerodynamic flow control are referred to the recent comprehensive reviews on the subject by Corke et al. [4] and Moreau [5].

One of the first applications of PSVGs for aerodynamic flow control was reported by Huang et al. [6] in which plasma-induced streamwise vorticity was used for aeroacoustic control of a low-speed cavity resonance. More recently, Schatzman and Thomas [7] demonstrated the efficacy of PSVGs to eliminate separation of an adverse pressure gradient turbulent boundary developing on a convex ramp. PSVGs were also found to be quite effective in eliminating unsteady

Presented as Paper 2012-0824 at the 50th AIAA Aerospace Sciences Meeting, Nashville, TN, 9–12 January 2012; received 15 October 2014; revision received 31 March 2015; accepted for publication 13 May 2015; published online 30 July 2015. Copyright © 2015 by the American Institute of Aeronautics and Astronautics, Inc. All rights reserved. Copies of this paper may be made for personal or internal use, on condition that the copier pay the \$10.00 per-copy fee to the Copyright Clearance Center, Inc., 222 Rosewood Drive, Danvers, MA 01923; include the code 1533-385X/15 and \$10.00 in correspondence with the CCC.

\*Graduate Research Assistant, Department of Aerospace & Mechanical Engineering, Institute for Flow Physics and Control, Member AIAA.

<sup>†</sup>Department of Aerospace & Mechanical Engineering, Institute for Flow Physics and Control, Associate Fellow AIAA.

<sup>‡</sup>Clark Equipment Professor, Department of Aerospace & Mechanical Engineering, Institute for Flow Physics and Control, Fellow AIAA.

<sup>§</sup>Associate Fellow AIAA.

vortex shedding from a circular cylinder in crossflow at high sub-critical Reynolds numbers, as reported by Kozlov and Thomas [8], and in the aeroacoustic control of a tandem cylinder flow configuration by Kozlov and Thomas [9]. Okita et al. [10] reported delayed separation on a NACA 0024 airfoil due to the streamwise vortex produced by a single, yawed DBD actuator, which essentially functioned as a PSVG. Motivated by wind turbine applications, Jukes et al. [11] applied PSVG arrays to a NACA 4418 airfoil for separation control. They reported a 65% reduction in form drag and an increase in lift coefficient of  $\Delta C_l = 0.4$  for experiments at a chord Reynolds number of 35,000.

A parametric investigation into DBD vortex generators was reported by Jukes and Choi [12]. The plasma vortex generator geometry used in that study was different from that used in this paper. It consisted of a single DBD plasma actuator whose surface electrode was placed at a yawed angle with respect to the oncoming flow direction. The plasma-induced spanwise wall jet interacted with the laminar boundary-layer flow to produce a streamwise vortex whose subsequent evolution was examined via particle image velocimetry (PIV) in local crossflow planes. DBD actuators producing both corotating and counter-rotating vortices were demonstrated. The effect of plasma-induced velocity, freestream velocity, surface electrode yaw angle, and length were systematically investigated. The benefits of electrode length and a yaw angle orthogonal to the oncoming flow were documented. The mechanism of streamwise vortex formation in a single electrode DBD plasma vortex generator was the topic of Jukes and Choi [13]. They found that a reorientation of laminar boundary-layer spanwise vorticity into the outer shear layer of the plasma-induced spanwise wall jet, combined with the considerable streamwise vorticity already present in the jet shear layer, was responsible for streamwise vortex formation.

Based upon the literature cited earlier, the efficacy of PSVGs for flow control has been demonstrated. In this paper, an experimental investigation into basic mechanisms governing the behavior of PSVG actuator arrays is presented. The focus of the work is to 1) gain a better understanding of the mechanism of vorticity generation and 2) to derive and experimentally verify scaling relations for these devices. The understanding gleaned from this investigation is considered a prerequisite to optimizing PSVG arrays for specific flow control applications.

The PSVG arrays are flush mounted to a flat plate on which a nominally zero pressure gradient (ZPG) turbulent boundary layer develops. Unlike the study by Jukes and Choi [12,13], which used a thin, 250  $\mu\text{m}$  Mylar dielectric barrier, this study exploits the work of Thomas et al. [14], which demonstrated a better than order-of-magnitude increase in the plasma-induced body force produced by actuators using comparatively thick dielectric barriers. Consequently, the PSVGs in this study use a quartz dielectric of 3.18 mm (1/8 in.) thickness ( $\approx 13$  times thicker than in [12,13]). This allows the application of much higher ac voltages than is possible with plasma actuators using thin-film dielectric barriers (in this case, up to 50 kV peak-to-peak). In fact, the lowest applied voltage in this study exceeded the maximum voltage of 12 kV peak-to-peak used in [12]. This is significant because it has been shown [4,14] that the body

force scales with the applied voltage to the  $7/2$  power. The PSVG array geometric design in this study is also very different than the single yawed DBD actuators used in [12,13], as detailed in the following section. Furthermore, the approach boundary layer is fully turbulent and the freestream flow velocity in the present study extends to 35 m/s, whereas most of the experimental results presented in [12] are for laminar boundary layers with very low freestream velocities (less than 2 m/s). Perhaps more significantly, the ratio of plasma-induced jet velocity  $\bar{W}_P$  to freestream velocity  $U_\infty$  was as high as 1.2 in [12]. In the current study, the values are  $0.03 \leq \bar{W}_P/U_\infty \leq 0.07$  (two orders of magnitude smaller).

## II. Experimental Apparatus and Procedures

### A. Wind-Tunnel Facility

The PSVG experimental investigation was performed in one of the low-turbulence, subsonic in-draft wind tunnels located at the Hesert Laboratory for Aerospace Research at the University of Notre Dame. The wind tunnel has an inlet contraction ratio of 20:1. A series of 12 turbulence management screens at the front of the inlet give rise to tunnel freestream turbulence levels of less than 0.1% (0.06% for frequencies above 10 Hz). The maximum tunnel speed is approximately  $U_\infty = 40$  m/s. Experiments are performed in a test section of 0.61 m (2 ft.) square cross-section and 1.82 m (6 ft) in length. One test section and the ceiling have optical access for nonintrusive laser flowfield diagnostics [in this study, laser Doppler anemometry (LDA) or PIV].

### B. Experimental Test Fixture

A schematic of the test fixture is shown in Figs. 1a and 1b, whereas Fig. 1c presents a rendered CAD model. The PSVG test fixture consists of a flat acrylic boundary-layer development plate that is 1.2 m (48 in.) in length, 0.6 m (24 in.) in width, and 1 cm (0.4 in.) thick with a rounded leading-edge containing distributed sand grain roughness to promote rapid boundary-layer transition (labeled 1 in Fig. 1). The last 0.2 m length of the plate consists of a 2.2 deg linear, symmetric taper down to a trailing-edge thickness of 1.6 mm (labeled 2 in Fig. 1). The plate was sidewall mounted and spanned the wind-tunnel test section. As shown in Fig. 1, a PSVG actuator test fixture (labeled 3 in Fig. 1) was flush mounted into a cavity machined into the plate surface at a location 0.79 m (31 in.) downstream of the leading-edge. This streamwise distance from the leading-edge allows for nominally ZPG turbulent boundary-layer growth before application of PSVG flow control. The cavity provides ample room for accommodating both the required high-voltage leads and the dielectric barrier material that forms the PSVG. Figure 2c shows a close-up view of one of the PSVG arrays ready for installation into the plate cavity. A full description of the PSVG geometry and details regarding construction are presented in the following section.

### C. Plasma Streamwise Vortex Generator Array

The basic geometry of the PSVG arrays examined in this study is shown schematically in Fig. 2. As indicated in the figure, this configuration uses a common covered electrode, which is separated

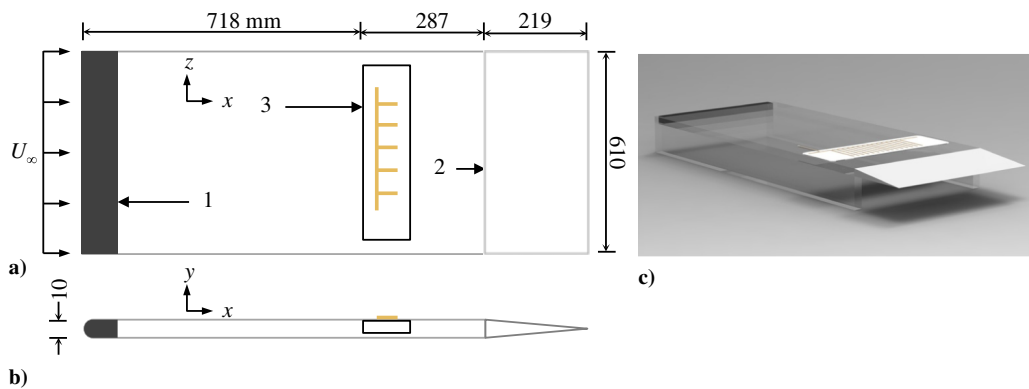


Fig. 1 Experimental test fixture: a) top view schematic, b) side view schematic, and c) rendered CAD model.

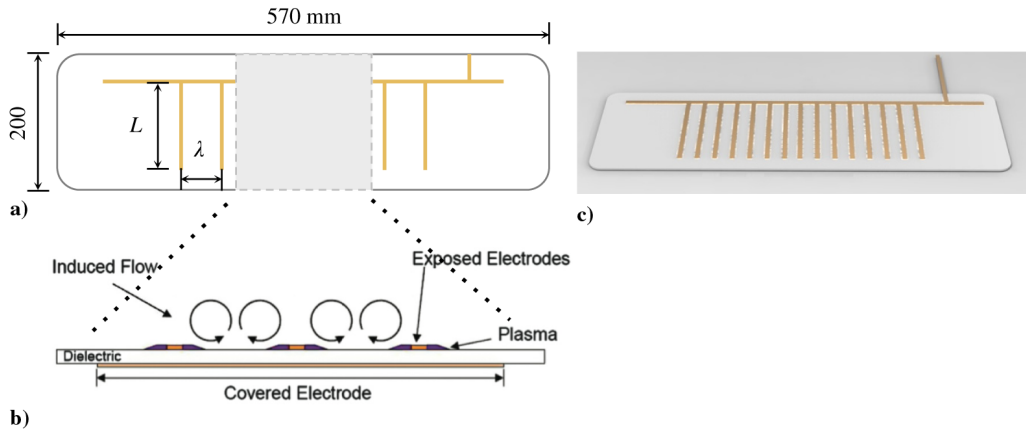


Fig. 2 Schematic of PSVG array geometry: a) top view, b) streamwise view, and c) close up of a PSVG array insert.

from the exposed electrodes by a sheet of dielectric barrier material. The multiple exposed (surface) electrodes with streamwise length  $L$  and spanwise interelectrode spacing  $\lambda$  are aligned parallel to the oncoming flow. Because of the use of a common covered electrode, plasma forms on both sides of each surface electrode. It will be shown that the resulting body force gives rise to a series of opposing wall jets in the spanwise direction that collide and interact with the external flow, thereby generating pairs of counter-rotating streamwise vortices with size  $O(\lambda/2)$  as indicated in Fig. 2b. These become the basis for enhanced cross-stream mixing of momentum within the boundary layer for separation control. The electrode array shown in Fig. 2 for the generation of streamwise vorticity is obviously quite different from the single streamwise-oriented DBD actuator investigated by Jukes and Choi [13].

As noted earlier, the dielectric material used in this study was quartz of 3.2 mm thickness (1/8 in.). The dielectric material extended 0.57 m (22.5 in.) in the spanwise direction and 20.3 cm (8 in.) in the streamwise direction. Each plasma actuator electrode consisted of copper foil tape of 0.05 mm thickness. Each of the streamwise-oriented exposed electrodes extended from a common spanwise surface electrode upstream of the covered electrode, as shown in Fig. 2a (no plasma forms on this spanwise electrode). In each case, the span was fixed at 46.4 cm (18.25 in.). Each exposed electrode is 3.2 mm (1/8 in.) in width and has a length of 15.24 cm (6 in.). The streamwise length of the covered electrode was varied in this investigation. This controlled the streamwise extent of the plasma forming region on each surface electrode. Streamwise lengths of 2.54, 5.08, 10.2, and 15.24 cm (1, 2, 4, and 6 in.) were examined.

Both the covered electrode and exposed electrode were connected to high-voltage wires that led out of the test fixture and connected to the transformers of the plasma generation circuit. The circuit used to operate the PSVG array is identical to that presented in Kozlov and Thomas ([8] Fig. 6). Unless otherwise noted, the actuators were operated with an ac carrier consisting of a sinusoidal waveform of 2 kHz frequency and a peak-to-peak voltage that was varied from 15 to 50 kV.

#### D. Flowfield Diagnostics

This study used standard, nonintrusive flowfield diagnostics in the form of LDA and PIV to characterize the vorticity generation by the PSVG arrays. These techniques are briefly described in this section.

LDA surveys of mean velocity in  $y-z$  crossflow planes were obtained both over and downstream of the PSVG arrays using a Dantec Dynamics Fiber Flow LDA system with a Spectra Physics Stabilite 2017 Argon-Ion Laser. The LDA system allows for cross-flow plane measurements of mean velocity at high freestream flow speeds, which would otherwise not be feasible with conventional planar or stereo PIV due to the dominant out-of-plane (streamwise)  $x$ -velocity component. The fiber optic LDA system was operated in full 180 deg backscatter mode. The Doppler bursts were measured using a BSA F60 flow processor and BSA Flow Software Version 4.10. The boundary-layer flow was seeded with Di-Ethyl-Hexyl-Sebacate (DEHS) particles of nominally 1  $\mu\text{m}$  diameter that were introduced

upstream of the wind-tunnel inlet contraction with a TSI Six-Jet Atomizer 9306.

At each streamwise measurement location, the fiber optic probe (using a 400 mm focal length lens) was traversed in a rectangular  $30 \times 25$  mm grid in the local  $y-z$  crossflow plane using a three-axis Aerotech traverse system and Unidex 11 controller. The LDA probe measurement volume has a maximum wall-normal dimension of 0.38 mm and just over 1.3 mm in the spanwise direction. This effectively set the spatial resolution for the mean flow measurement.

The  $\bar{U}$ ,  $\bar{V}$ , and  $\bar{W}$  mean velocity components were measured in a given cross-stream plane via two measurements at each  $y-z$  location. These were performed with the LDA transceiver head oriented at two separate oblique angles  $\alpha_1$ , and  $\alpha_2$  (with respect to the boundary-layer development plate surface). A coordinate transformation related the measured mean velocities  $\bar{U}_1$ ,  $\bar{U}_2$ , and  $\bar{U}_3$  to measurements of  $\bar{U}$ ,  $\bar{V}$ , and  $\bar{W}$ . In particular,

$$\begin{bmatrix} \bar{U}_1 \\ \bar{U}_2 \\ \bar{U}_3 \end{bmatrix} = \begin{bmatrix} 1 & 0 & 0 \\ 0 & \cos(\alpha_1) & \sin(\alpha_1) \\ 0 & \cos(\alpha_2) & \sin(\alpha_2) \end{bmatrix} \begin{bmatrix} \bar{U} \\ \bar{V} \\ \bar{W} \end{bmatrix} \quad (1)$$

The last two equations of Eq. (1) allow  $\bar{V}(x; y, z)$  and  $\bar{W}(x; y, z)$  to be determined from measured  $\bar{U}_2(x; y, z)$  and  $\bar{U}_3(x; y, z)$ . The estimated relative uncertainty in the mean flow measurements at 20:1 odds was estimated to be  $\pm 3.4\%$ .

For mean flow measurements without external flow, a LaVision time-resolved PIV system was used to nonintrusively acquire two-component velocity data in selected  $y-z$  planes. The system consisted of a Litron LDY300 series neodymium-doped yttrium lithium fluoride pulse laser, a Photron SA 1.1 high-speed camera, and dedicated computer running DaVis 8.0 vector processing software. The laser light sheet was directed through the side window of the wind tunnel. Sheet optics consisting of a combination of a spherical and a cylindrical lens were used to create a 1-mm-thick light sheet at the measurement plane. The high-speed camera, equipped with a Nikon 105 mm lens and 2x teleconverter operating at  $f2.8$ , was positioned on top of the test section, angled at approximately 30 deg to the actuator surface. This angular distortion was corrected with an appropriately aligned calibration plate, and calibrations were performed at each discrete  $x$  position. The interrogation region corresponded to physical domains of approximately  $48-57 \times 59-65$  mm, depending on the calibration used. A TSI atomizer produced nominally 1- $\mu\text{m}$ -diam DEHS seed particles injected upstream of the wind-tunnel inlet via a mixing box, allowing for uniform particle dispersion in the measurement plane. The measurement uncertainty for the mean velocity and vorticity as measured with the PIV is estimated to be within 2 and 8%, respectively.

It should be noted that, for the electric fields encountered in these experiments, dimensional analysis confirms that the aerodynamic forces on the DEHS seed particles were several orders of magnitude greater than the electrostatic forces. Consistent with this, none of the LDA or PIV results suggested that seed particles follow electric field lines.

**Table 1** Upstream boundary-layer parameters

$U_\infty$ , m/s	$Re_x \times 10^6$	$\delta_{99\%}$ , mm	$\delta^*$ , mm	$\theta$ , mm	$H$	$C_f$
15	0.75	34.8	4.93	3.57	1.38	0.0036
20	1.01	32.0	4.90	3.55	1.38	0.0034
25	1.26	31.4	4.87	3.52	1.38	0.0033
30	1.47	30.3	4.83	3.54	1.36	0.0033

### E. Approach Turbulent Boundary-Layer Flow

The approach ZPG turbulent boundary-layer mean velocity profiles all showed excellent agreement with the Klebanoff [15] profile (obtained at much higher  $Re_x$ ) as shown in Fig. 3 for a range of freestream velocities used in the experiment. Approach boundary-layer parameters are summarized in Table 1. It should be noted that shape factor and skin friction coefficient values were consistent with those for ZPG turbulent boundary layers at the given  $Re_x$ .

## III. Experimental Results

In this section, key results from the experimental investigation into the behavior of several PSVG arrays are presented. Before presenting results for the PSVG operated with an approach turbulent boundary-layer flow, consideration is first given to the case of no external flow.

### A. Quiescent Case Vorticity Generation

Before examining the interaction of the PSVG array with the oncoming boundary-layer flow, it is useful to consider how the actuators produce vorticity in the absence of an approach flow. To do this, PIV measurements of the actuator-induced flow were performed

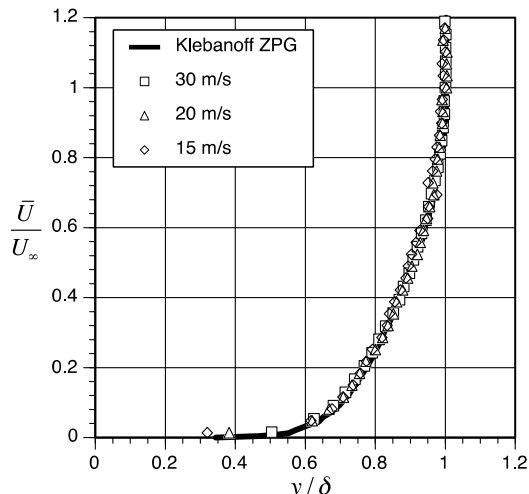


Fig. 3 Comparison of measured turbulent boundary-layer mean velocity profiles upstream of the PSVG array with that by Klebanoff [15].

in a  $y-z$  plane located at  $x = L/2$  to avoid end effects. In this section, representative results are presented that serve to illustrate the generation of  $x$ -oriented vortices by the PSVG array.

The plasma-induced wall-normal  $\bar{V}(x, y, z)$  and spanwise  $\bar{W}(x, y, z)$  mean velocity components were measured in the ( $x = L/2, y, z$ ) crossflow plane and these were used to compute the local  $x$ -component mean vorticity  $\bar{\omega}_x \equiv (\partial \bar{W} / \partial y - \partial \bar{V} / \partial z)$ , induced by the actuators in the absence of any external flow.

Figures 4a and 4b present representative measurements of  $\bar{V}(L/2, y, z)$  and  $\bar{W}(L/2, y, z)$ , respectively, for the case of an applied peak-to-peak voltage  $E_{pp} = 35$  kV, an interelectrode spacing  $\lambda = 25.4$  mm (1 in.), and covered electrode length  $L = 101.6$  mm (4 in.). For reference, the surface electrode locations are indicated as dark rectangles on the abscissa. Figure 4a shows measured  $\bar{V}(y, z)$  and indicates that the imposed actuator body force  $F_B = \rho_c E$  draws ambient fluid downward toward each surface electrode. This, combined with the impermeability of the wall, gives rise to a series of opposing spanwise wall jets as shown in the  $\bar{W}(y, z)$  measurements presented in Fig. 4b. The wall jets give rise to large values of  $\partial \bar{W} / \partial y$  near the wall.

The maximum spanwise wall jet velocity induced by the PSVG array is approximately  $\bar{W}_{p\max} \approx 1$  m/s. Experimental results presented in [14] for a comparable applied voltage and dielectric thickness show that this value of  $\bar{W}_{p\max}$  is approximately one-quarter to one-third of that which would be obtained for a conventional DBD plasma actuator in which plasma is allowed to form on only one side of the surface electrode. The reduced plasma-induced wall jet velocity for the PSVG is due to the (necessary) plasma formation on both sides of the surface electrode.

The opposing wall jets collide near the midpoint location between adjacent surface electrodes and this gives rise to a local upwelling of fluid, as shown in Fig. 4a. The maximum upwelling velocity is  $\bar{V}_{p\max} \approx 2.5$  m/s. The requirement of mass conservation leads to divergent spanwise mean velocity  $\bar{W}$  near the top of the upwelling. The wall-directed motion of fluid over the electrodes, combined with the localized upwelling between, also gives rise to large values of  $\partial \bar{V} / \partial z$ .

Figure 5 presents the isovelocity contours of the mean velocity induced by the PSVG array and clearly shows the spanwise periodic nature of the actuator-induced mean flow pattern. In this manner,  $x$ -component vorticity  $\bar{\omega}_x = (\partial \bar{W} / \partial y - \partial \bar{V} / \partial z)$  is created by the PSVG actuator as shown in the isovorticity contour map of Fig. 6. This figure clearly shows that a periodic array of counter-rotating  $x$ -oriented vortices is set up by the actuator-induced body force. Peak values of time-mean mean vorticity are observed to be approximately  $\bar{\omega}_x \approx 250$  s<sup>-1</sup>.

It is apparent from the measurements presented that the body force due to the actuator array acts in combination with the no-slip condition at the wall to produce  $x$ -directed vorticity in the quiescent case. However, it will be shown that the magnitude of peak  $x$ -directed (i.e., streamwise) vorticity is considerably larger when there is an

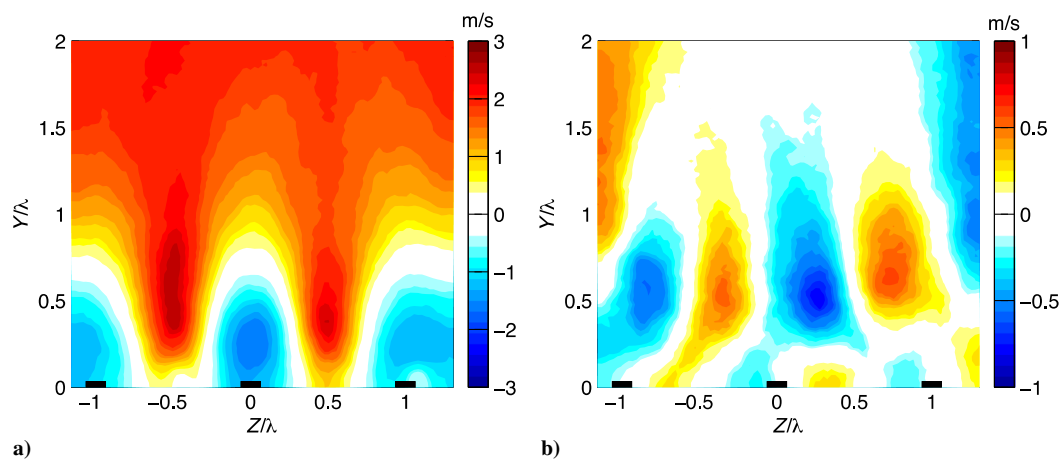


Fig. 4 Measured a)  $\bar{V}(y, z)$  and b)  $\bar{W}(y, z)$  induced by the PSVG array:  $V_{pp} = 50$  kV,  $\lambda = 25.4$  mm,  $L = 101.6$  mm,  $x/L = 0.5$ .

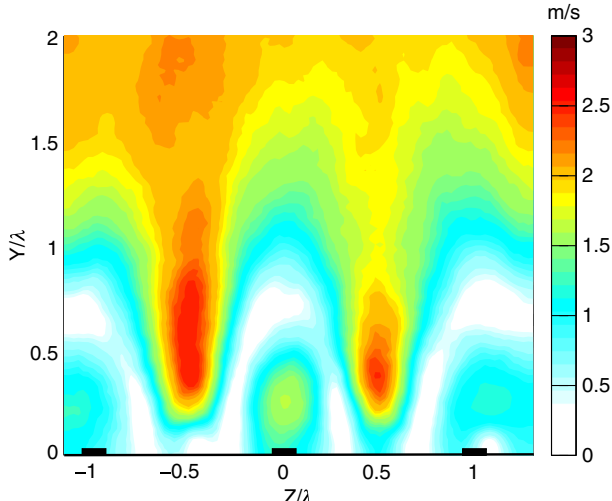


Fig. 5 Contours of PSVG actuator-induced velocity for the quiescent case:  $V_{pp} = 50$  kV,  $\lambda = 25.4$  mm,  $L = 101.6$  mm,  $x/L = 0.5$ .

approach turbulent boundary-layer flow. This suggests that a primary mechanism for PSVG vorticity production involves the interaction of the plasma-generated flow with the oncoming boundary layer. The nature of this interaction mechanism will be the focus of the next section.

#### B. Mechanism of PSVG Streamwise Vorticity Generation: Scaling Relations

In this section, consideration is given to the mechanism of streamwise vorticity generation by the PSVG array when there is an approach boundary-layer flow. Scaling arguments will be used to demonstrate that a key element in this process is the interaction of the approach boundary-layer flow with the plasma-induced flow set up by the actuator body force vector.

Figure 7 shows contours of the time mean streamwise vorticity  $\bar{\omega}_x$ , created at the downstream end of a PSVG array for the case in which there is an approach turbulent boundary-layer flow. In particular, contours of  $\bar{\omega}_x$  are presented in a  $y-z$  plane located at the downstream edge of the PSVG actuator for several values of freestream velocity,  $10 \text{ m/s} \leq U_\infty \leq 30 \text{ m/s}$  with  $L = 101.6$  mm,  $\lambda = 2.54$  cm,  $E_{pp} = 40$  kV, and  $x/L = 1$ . These data were acquired via laser Doppler anemometry using the method described in Sec. II.D. Figure 7 shows a qualitative resemblance to the mean vorticity field setup in the quiescent case described previously (see Fig. 6), but the reader will note that the streamwise vorticity magnitude produced with an approach boundary-layer flow is much larger. This indicates the important role played by the interaction with the approach boundary-

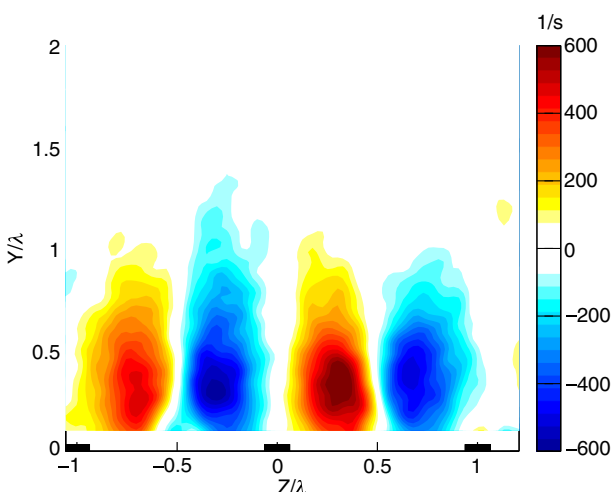


Fig. 6 Contours of  $x$ -directed vorticity produced by PSVG array in quiescent case:  $V_{pp} = 50$  kV,  $\lambda = 25.4$  mm,  $L = 101.6$  mm,  $x/L = 0.5$ .

layer flow. Note that the wall-normal coordinate is scaled by the local boundary-layer thickness  $\delta$ , and Fig. 7 indicates that the vortices are confined within the turbulent boundary layer. It is easy to show that, for a pair of potential vortices in proximity to a horizontal wall, there is a self-induced motion of the vortex pair in the wall-normal direction, which at fixed circulation  $\Gamma$  is directly proportional to time. In this experiment,  $L$  was fixed and  $U_\infty$  was varied and so, not surprisingly, Fig. 7 shows that the greatest wall-normal extent of streamwise vorticity is associated with the largest convective timescale  $L/U_\infty$ . For example, at  $U_\infty = 10$  m/s, streamwise vorticity extends to  $y/\delta \approx 0.4$ . Conversely, at the highest freestream speed and smallest convective timescale, the streamwise vorticity is largely confined to the near-wall region  $y/\delta \leq 0.15$ .

To examine the generation of mean streamwise vorticity  $\bar{\omega}_x$  by the PSVG array, consideration is given to the  $x$ -component mean vorticity transport equation, which is given by

$$\frac{D\bar{\omega}_x}{Dt} = \bar{\omega}_j \bar{S}_{xj} + \overline{\omega'_j s_{xj}} - u_j \overline{\frac{\partial \omega'_x}{\partial x_j}} + \nu \frac{\partial^2 \bar{\omega}_x}{\partial x_j \partial x_j} \quad (2)$$

The actuator array is operated in a quasi-steady manner and focus will be given to its influence on the time mean flow as illustrated in Fig. 7. In this context, the primary streamwise vorticity generation occurs through the mean vorticity-strain rate interaction terms  $\bar{\omega}_j \bar{S}_{xj}$ . In contrast, the vorticity fluctuation-fluctuating strain rate correlation  $\overline{\omega'_j s_{xj}}$  and fluctuating velocity-vorticity gradient correlation  $u_j \overline{\partial \omega'_x / \partial x_j}$  on the right-hand side of Eq. (2) are largely responsible for turbulent vorticity redistribution mechanisms that occur within the boundary layer downstream of the actuator. Further, viscous diffusion is neglected because, for high Reynolds number flow, it operates on timescales that are much longer than the mean vorticity-mean strain rate interaction terms. Hence, focus is given to the terms

$$\bar{\omega}_j \bar{S}_{xj} = \bar{\omega}_x \bar{S}_{xx} + \bar{\omega}_y \bar{S}_{xy} + \bar{\omega}_z \bar{S}_{xz} \quad (3)$$

In the nominally zero-pressure gradient turbulent boundary layer under consideration here, streamwise dilatation is negligible,  $\bar{S}_{xx} = 0$ . Hence, focus is given to the two remaining terms,  $\bar{\omega}_y \bar{S}_{xy} = \bar{\omega}_y \partial \bar{U} / \partial y$  and  $\bar{\omega}_z \bar{S}_{xz} = \bar{\omega}_z \partial \bar{U} / \partial z$ . The former term serves to take wall-normal mean vorticity and reorient it into the streamwise direction. The latter term does the same for initially spanwise-oriented mean vorticity.

The wall-normal time mean vorticity  $\bar{\omega}_y \equiv \partial \bar{U} / \partial z - \partial \bar{W} / \partial x$  in the zero pressure gradient turbulent boundary layer upstream of the actuator is expected to be negligible, and this was confirmed experimentally. However, as shown in the sample  $\bar{U}(y, z)$  isocontour measurements obtained at the downstream edge of the PSVG array presented in Fig. 8, the plasma-induced body force draws ambient fluid toward the surface electrodes and also gives rise to wall-normal flow away from the wall at locations midway between adjacent electrodes. The combined effect serves to create wall-normal vorticity through the production of nonzero  $\partial \bar{U} / \partial z$ .

To further characterize  $\partial \bar{U} / \partial z$ , the LDV probe volume was traversed in the spanwise  $z$  direction at a fixed distance of 7.62 cm (3 in.) downstream of the PSVG array, with the wall-normal height fixed at  $\delta^*$ , the local boundary-layer displacement thickness. Figure 9 presents the spanwise variation of mean velocity  $\bar{U}(\delta^*, z)$  downstream of the PSVG array for external velocities ranging from  $10 \leq U_\infty \leq 30$  m/s (corresponding to the Reynolds number range of  $0.54 \text{ million} \leq Re_x \leq 1.61 \text{ million}$ ). Traverses at several other wall-normal locations were also performed, and the results in Fig. 9 may be considered representative. The spanwise variation is observed to be quasi periodic. To account for the variation in external velocity between trials, the measurements are presented by subtracting the spanwise cycle-average mean velocity  $\langle \bar{U} \rangle$  and normalizing by the external velocity  $U_\infty$ . The location  $z = 0$  is centered midway between adjacent surface electrodes (electrode locations are shown on the abscissa). Figure 9 shows that this normalization provides a remarkable collapse for all the cases. Negative peaks are centered

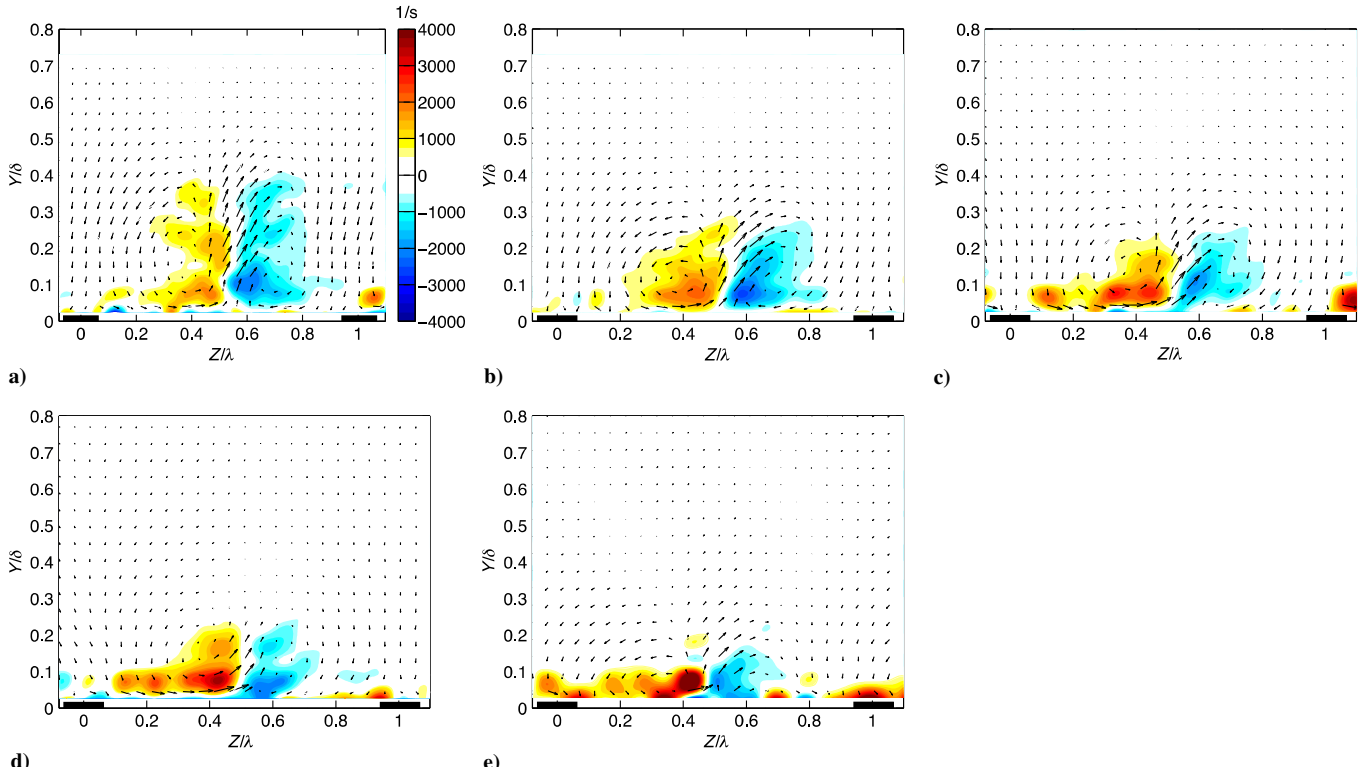


Fig. 7 Mean streamwise vorticity contours and velocity vectors at  $U_{\infty}$  = a) 10, b) 15, c) 20, d) 25, and e) 30 m/s. PSVG electrodes drawn schematically in black.

between the surface electrodes and are associated with the local upwelling of comparatively low-velocity fluid from the near-wall region due to colliding spanwise plasma-induced wall jets (as also seen in Fig. 8). In contrast, broader positive excursions are centered over the surface electrodes and are associated with transport of comparatively high-velocity fluid downward toward the surface electrodes by the plasma-induced body force. Because of the similarity scaling demonstrated in Fig. 9, the ordinate may be denoted as  $F(z)$ , and it follows that  $\partial \bar{U} / \partial z = U_{\infty} dF / dz$ . That is, the spanwise mean velocity gradient set up by the PSVG array  $\partial \bar{U} / \partial z$  is directly proportional to  $U_{\infty}$ . This aspect will be used in scaling arguments developed later in this section.

As a consequence of the spanwise mean velocity gradient set up by the PSVG array, we have  $\bar{\omega}_y \bar{S}_{xy} \approx (\partial \bar{U} / \partial z)(\partial \bar{U} / \partial y)$ . Consider next the term  $\bar{\omega}_z \bar{S}_{xz} \approx \bar{\omega}_z \partial \bar{U} / \partial z$ . To good approximation, the mean

spanwise vorticity in the turbulent boundary layer is  $\bar{\omega}_z \approx \partial \bar{U} / \partial y$ . Hence, we have  $\bar{\omega}_z \bar{S}_{xz} \approx (\partial \bar{U} / \partial y)(\partial \bar{U} / \partial z)$ , and so it follows that both of the relevant vorticity-strain rate interaction terms involve the product of mean velocity gradients in the wall-normal and spanwise directions. For the vorticity redistribution mechanism, the required  $\partial \bar{U} / \partial y$  is provided primarily by the approach boundary-layer flow, whereas the plasma-induced body force associated with the PSVG array creates the required spanwise gradients in mean velocity  $\partial \bar{U} / \partial z$ , as illustrated in Figs. 8 and 9.

The approach turbulent boundary-layer mean spanwise vorticity

$$\bar{\omega}_z = \frac{\partial \bar{U}}{\partial y} \approx O\left(\frac{U_{\infty}}{\delta^*}\right) \quad (4)$$

where  $\delta^*$  is the displacement thickness (i.e., the wall-normal centroid of spanwise vorticity for the turbulent boundary layer). This is an intermediate strain rate scaling that is much less than the limiting

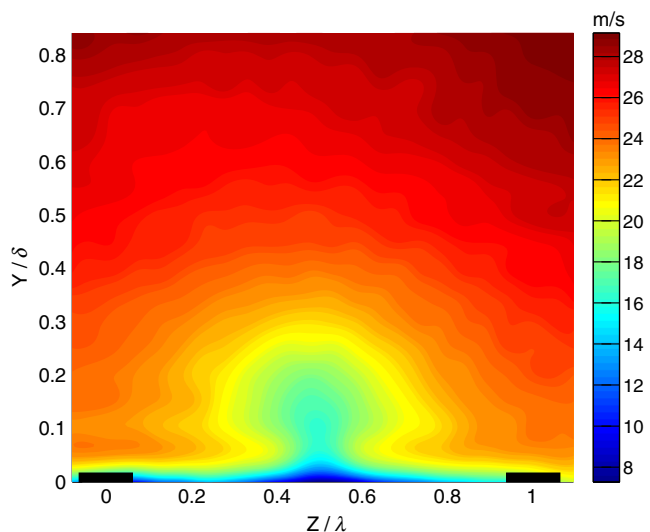


Fig. 8 Streamwise mean velocity contours measured at downstream edge of PSVG array for case of  $U_{\infty} = 30$  m/s,  $E_{pp} = 40$  kV,  $\lambda = 25.4$  mm,  $x/L = 1$ ,  $L = 101.6$  mm.

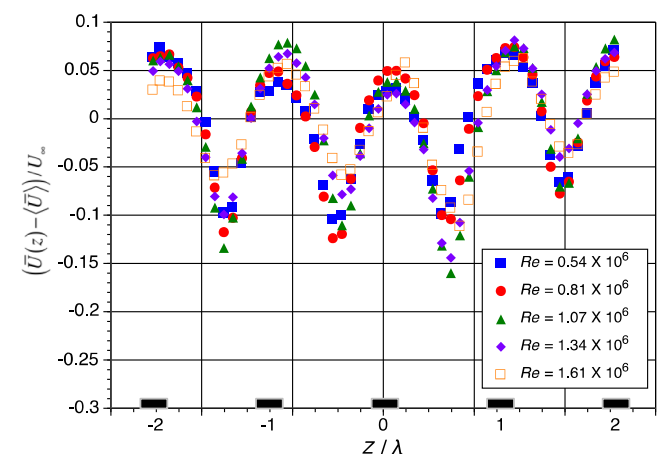


Fig. 9 Spanwise variation of scaled streamwise-component mean velocity downstream of PSVG array (40 kV case); surface electrode location indicated on abscissa.

value near the wall,  $u_r^2/\nu$ . It has been shown that the PSVG array sets up a spanwise mean velocity gradient

$$\frac{\partial \bar{U}}{\partial z} \approx O\left(\frac{\Delta \bar{U}}{\lambda}\right) \quad (5)$$

where  $\lambda$  is the spanwise interelectrode spacing and  $\Delta \bar{U}$  is a characteristic change in the streamwise velocity component. Hence, we have the following scaling for the mean vorticity redistribution terms:

$$\bar{\omega}_y \frac{\partial \bar{U}}{\partial y} = \bar{\omega}_z \frac{\partial \bar{U}}{\partial z} \approx O\left(\frac{U_\infty}{\delta^*} \frac{\Delta \bar{U}}{\lambda}\right) \quad (6)$$

Based on measurements presented in Fig. 9, we know that

$$\partial \bar{U} / \partial z \approx U_\infty F(z) \approx O(\Delta \bar{U} / \lambda) \quad (7)$$

Hence, we have

$$\bar{\omega}_y \frac{\partial \bar{U}}{\partial y} = \bar{\omega}_z \frac{\partial \bar{U}}{\partial z} \approx O\left(\frac{U_\infty^2}{\delta^*} F(z)\right) \quad (8)$$

We could also obtain a similar result via an analogy to the turbulent mixing length concept. Expanding the wall-normal variation in mean velocity in a Taylor series, we have, to leading order,

$$\bar{U}(y + \ell_p) \approx \bar{U}(y) + \frac{\partial \bar{U}}{\partial y} \Big|_y \ell_p(z) \quad (9)$$

where  $\ell_p(z)$  is a characteristic wall-normal distance that “fluid parcels” are displaced by the actuator array. Hence,

$$\Delta \bar{U} \approx \frac{\partial \bar{U}}{\partial y} \Big|_y \ell_p \approx O\left(\frac{U_\infty}{\delta^*} \ell_p(z)\right) \quad (10)$$

which leads to

$$\bar{\omega}_y \frac{\partial \bar{U}}{\partial y} = \bar{\omega}_z \frac{\partial \bar{U}}{\partial z} \approx O\left(\frac{U_\infty^2}{\delta^{*2}} \ell_p(z)\right) \quad (11)$$

Comparison of Eqs. (8) and (11) along with Fig. 9, suggests that  $F(z) \approx \ell_p(z)/\delta^* \approx O(0.1)$

Since

$$\frac{D\bar{\omega}_x}{Dt} \approx O\left(\frac{\Delta \bar{\omega}_x U_\infty}{L}\right)$$

it follows that the increase in streamwise vorticity  $\Delta \bar{\omega}_x$  occurring over a PSVG actuator of length  $L$  is

$$\Delta \bar{\omega}_x \approx O\left(\frac{\ell_p(z)L}{\delta^{*2}\lambda} U_\infty\right) \quad (12)$$

This relation indicates that the mean streamwise vorticity induced by an array of active length  $L$  should scale linearly with freestream velocity due to vorticity-strain rate interaction mechanisms. Similarly, for fixed  $U_\infty$ , the streamwise vorticity increment will be proportional to the covered electrode length  $L$ .

In the following sections, the validity of this scaling is experimentally examined. To most appropriately characterize the time mean streamwise vorticity produced by the PSVG  $\bar{\omega}_x \equiv (\partial \bar{W} / \partial y - \partial \bar{V} / \partial z)$ , a temporal and local spatially averaged value was taken. In particular, the time mean vorticity at a particular streamwise location  $x$ ,  $\bar{\omega}_x(y, z)$ , which is a point function, was also spatially averaged over the vortex area  $A_V$  in the local  $y-z$  plane, which was defined as the area surrounding the maximum vorticity location and bounded by the locus of points where the streamwise vorticity has fallen to 10% of

the local maximum value. Other thresholds were used and results based on the 10% threshold may be considered representative. The circulation associated with time mean streamwise vorticity

$$\Gamma \equiv \iint_{A_V} \bar{\omega}_x \, dA_V \quad (13)$$

is also used to characterize the actuator performance. Here  $A_V$  represents the vortex area in the  $y-z$  plane as defined earlier.

### C. Effect of Freestream Velocity

Measurements were made to examine the validity of the scaling of  $\bar{\omega}_x$  with  $U_\infty$ . Figure 10 presents the variation of  $\bar{\omega}_x$  associated with one of the streamwise vortices produced by the PSVG as a function of  $U_\infty$ . The measurements were made at the downstream edge of the PSVG array. The experimental conditions correspond to the data set presented in Fig. 7. This figure clearly shows that  $\bar{\omega}_x \propto U_\infty$  as suggested by the previous scaling argument. Also shown for reference in the figure is the mean streamwise vorticity measured at the same actuator voltage for the no-external-flow case. It is clear that mean vorticity-strain rate interaction terms serve to increase the streamwise vorticity produced by the array, as suggested in the previous scaling analysis. Figure 10 shows that that PSVGs harvest energy from the external flow and exhibit an increase in actuator effectiveness with flow speed that makes the PSVG unique among DBD plasma flow control devices. The conditions required for this behavior are discussed in the following sections.

Figure 11 presents the variation with freestream velocity of mean circulation associated with a single streamwise vortex as measured at the downstream edge of the PSVG array. These data correspond to

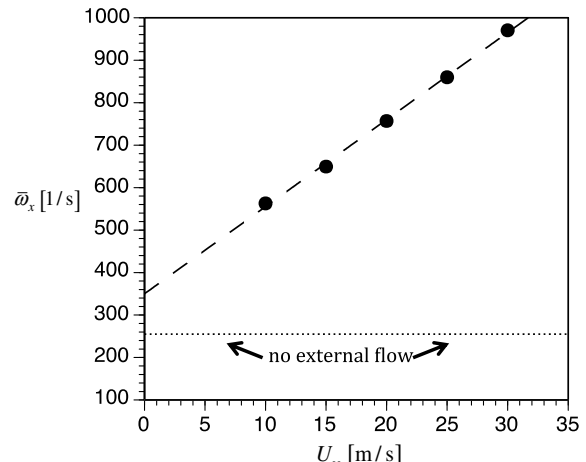


Fig. 10 Variation of mean streamwise vorticity with freestream velocity as measured at downstream edge of PSVG array (conditions correspond to those in Fig. 7).

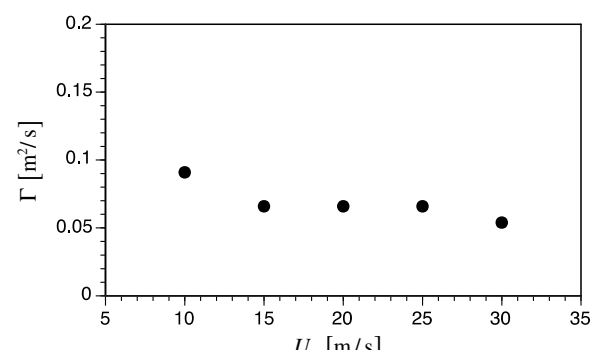


Fig. 11 Variation of mean streamwise circulation with freestream velocity as measured at downstream edge of PSVG array (conditions correspond to those in Fig. 7).

conditions identical to those for Fig. 7. Figure 11 shows that the circulation varies only weakly with  $U_\infty$ . This is fully consistent with the previous result for  $\bar{\omega}_x$  shown in Fig. 10 because measurement of the associated vortex area  $A_V$ , (defined as that surrounding the local streamwise vorticity maximum and bounded by the locus of points where the streamwise vorticity has dropped to 10% of the local maximum) varies as  $U_\infty^{-1}$ . For fixed covered electrode length  $L$  this indicates that the vortex area varies in proportion to the convective timescale  $T_C \equiv L/U_\infty$ .

#### D. Relevant Timescales

It has been shown that the production of streamwise vorticity by the PSVG array depends upon vorticity redistribution mechanisms, and these will require a certain minimum residence time of fluid particles over the actuator. The relevant timescales are the convective timescale  $T_C \equiv L/U_\infty$  and the inverse mean strain rates  $S_{xy}^{-1}$  and  $S_{xz}^{-1}$ . The timescale  $S_{xy}^{-1}$  is set by the approach boundary layer and  $S_{xz}^{-1}$  by the PSVG array. For the actuator to be maximally effective, it must be that  $T_C \geq S_{xy}^{-1}$  and  $T_C \geq S_{xz}^{-1}$ . For the experimental results shown in Figs. 7, 10, and 11 the convective timescale varied from  $3.4 \text{ ms} \leq T_C \leq 10.2 \text{ ms}$ , whereas  $0.5 \text{ ms} \leq S_{xy}^{-1} \leq 0.2 \text{ ms}$  and  $1.4 \text{ ms} \leq S_{xz}^{-1} \leq 3.9 \text{ ms}$ . It follows that the convective timescale was always greater than the inverse strain rate timescales in the experiments. Furthermore, it is noted that  $S_{xy}^{-1} \ll S_{xz}^{-1}$ , which is expected to be generally true in turbulent boundary-layer flow control applications.

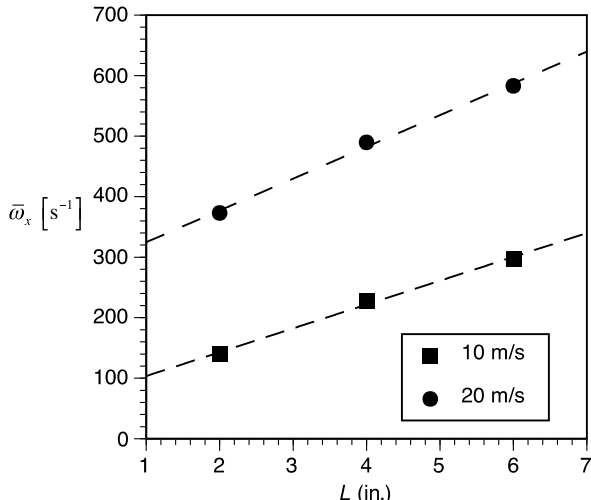


Fig. 12 Variation of  $\bar{\omega}_x$  with covered electrode length  $L$ .

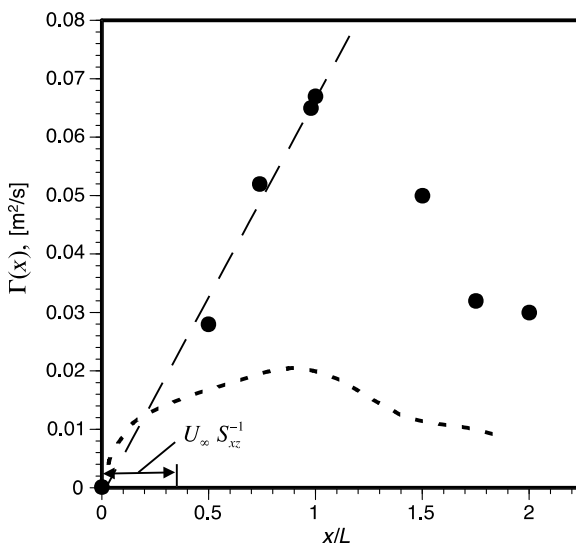


Fig. 13 Development of circulation  $\Gamma(x)$  over PSVG actuator (dark circles); (dashed line) single electrode plasma vortex generator from [13].

Hence, the primary operational constraint for the PSVG becomes  $T_C \geq S_{xz}^{-1}$ .

#### E. Effect of Actuator Length

The scaling relation (12) also indicates that the augmentation of mean streamwise vorticity at fixed  $U_\infty$  is directly proportional to the length of the active electrode  $L$ . Verification of this linear variation of  $\bar{\omega}_x$  with  $L$  is shown in Fig. 12, which presents the mean vorticity measured at a location 7.62 cm (3 in.) downstream of the PSVG array as a function of  $L$  for two representative values of  $U_\infty$ . To acquire these data, multiple PSVG arrays were constructed with covered surface electrode lengths of  $L = 5.08, 10.16$ , and  $15.24 \text{ cm}$  (2, 4, and 6 in.). In each case, the spanwise interelectrode spacing was kept fixed at  $\lambda = 2.54 \text{ cm}$  (1 in.), and the applied voltage was maintained at  $E_{pp} = 35 \text{ kV}$ . Figure 12 shows that  $\bar{\omega}_x$  varies linearly with  $L$ , which is fully consistent with the scaling relation (12).

Figure 13 presents the streamwise evolution of circulation  $\Gamma(x)$  associated with the production of streamwise vorticity by a PSVG array for the case of  $L = 4 \text{ in.}$ ,  $U_\infty = 20 \text{ m/s}$ , and  $E_{pp} = 40 \text{ kV}$ . The streamwise length scale associated with the establishment of a spanwise mean velocity gradient  $U_\infty S_{xz}^{-1}$  is indicated in the figure. As expected, the circulation exhibits its peak value at the downstream edge of the actuator. Furthermore, the development of circulation

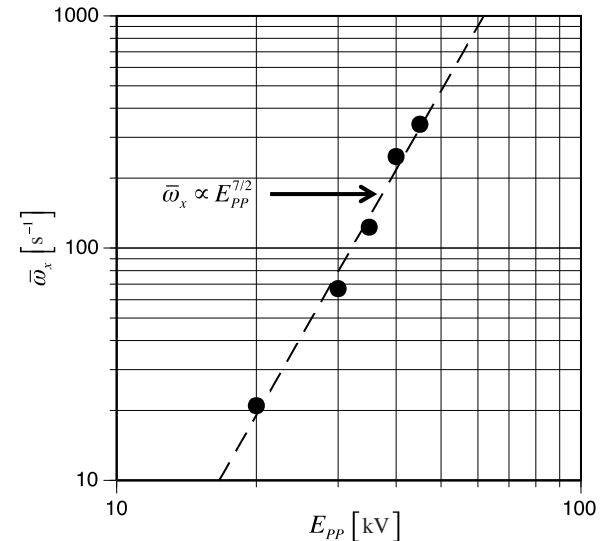


Fig. 14 Measured variation of  $\bar{\omega}_x$  with actuator applied voltage for  $L = \lambda = 2.53 \text{ cm}$  (1 in.),  $U_\infty = 20 \text{ m/s}$ .

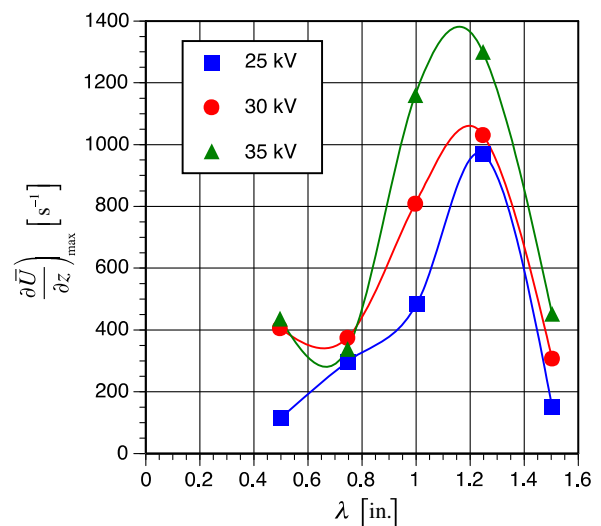


Fig. 15 Variation in  $\partial \bar{U} / \partial z|_{\max}$  as a function of PSVG interelectrode spacing  $\lambda$ .

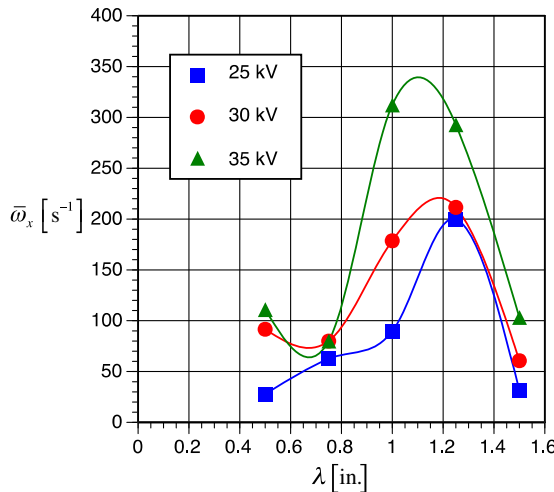


Fig. 16 Variation in  $\bar{\omega}_x$  as a function of PSVG interelectrode spacing  $\lambda$ .

exhibits a linear variation with streamwise distance  $x$  for locations over the actuator consistent with the scaling relation (12). Downstream of the actuator,  $\Gamma(x)$  diminishes due to turbulent vorticity redistribution within the boundary layer. The dashed curve in Fig. 13 shows the circulation development for the single electrode plasma vortex generator as reported in Jukes and Choi ([13] fig. 14). Aside from geometric differences in actuator geometry, the much lower peak circulation value is also consistent with the fact that spanwise vorticity redistribution mechanisms were not the primary source of streamwise vorticity production in that study. In fact, the spanwise vorticity in the approach turbulent boundary layer of the current study was 10–20 times (depending on the external flow speed) the vorticity in the laminar boundary layer of [13]. Note also that the decay of circulation downstream of the actuator is more gradual in [13] due to the laminar boundary-layer flow. In that case, turbulent vorticity redistribution mechanisms are not involved.

#### F. Effect of Applied Voltage

It is well known that the body force produced by DBD plasma actuators scale with applied voltage to the  $7/2$  power. This scaling is embodied in current state-of-the-art actuator models (Corke et al. [4]) and has also been demonstrated experimentally (see Thomas et al. [14] fig. 5). In this section, consideration is given to how the streamwise vorticity produced by a PSVG array varies with applied actuator voltage. Figure 14 presents experimental results that document this aspect. In particular, this figure shows the variation of  $\bar{\omega}_x$  with  $E_{pp}$  as measured at a location 7.62 cm (3 in.) downstream of a PSVG actuator with  $L = \lambda = 2.53$  cm (1 in.). The freestream velocity was fixed at the intermediate value of  $U_\infty = 20$  m/s. A least-squares power-law fit to the variation of  $\bar{\omega}_x$  with  $E_{pp}$  shows clearly that  $\bar{\omega}_x \propto E_{pp}^{3.5}$ . Because actuator body force scales with  $E_{pp}^{3.5}$ , this also indicates that the streamwise vorticity produced by the PSVG array scales with the magnitude of the body force  $|F_B|$ . This is consistent with the vorticity redistribution mechanism described previously,

where it was shown that the streamwise vorticity increment provided by the PSVG depends proportionately upon the spanwise velocity gradient  $\partial \bar{U} / \partial z$ , which, in turn, is set up by the body force vector.

#### G. Effect of Interelectrode Spacing

Experiments were performed to assess the effect of spanwise interelectrode spacing  $\lambda$  on the PSVG actuator performance. For these experiments, four separate PSVG arrays were constructed for installation into the test plate, in which in the interelectrode spacing was set at values of  $\lambda = 1.91, 2.54, 3.18$ , and  $3.81$  cm (0.75, 1.0, 1.25, and 1.5 in., respectively). In each case, the covered electrode length was kept fixed at  $L = 5.08$  cm (2 in.). Because it has been established that a key role of the PSVG array is to produce wall-normal vorticity through a spanwise mean velocity gradient  $\partial \bar{U} / \partial z$ , this quantity was measured downstream of each array, as was the mean streamwise vorticity  $\bar{\omega}_x$ .

Figure 15 presents values of  $(\partial \bar{U} / \partial z)_{MAX}$  as measured via LDA at a streamwise location 7.62 cm (3 in.) downstream of the actuator, as a function of PSVG interelectrode spacing  $\lambda$ . Results for three representative applied voltages are shown. In each case, there is clearly an optimum spacing of approximately  $\lambda_{OPT} \approx 3.2$  cm (1.2 in.). Note also that there is a rather abrupt reduction in  $(\partial \bar{U} / \partial z)_{MAX}$  for  $\lambda > \lambda_{OPT}$ .

Figure 16 presents measured values of  $\bar{\omega}_x$  as a function of PSVG interelectrode spacing  $\lambda$ . These data were acquired simultaneously with those presented in Fig. 15. Figure 16 clearly suggests that optimum performance of the PSVG in terms of mean streamwise vorticity production occurs for values of  $\lambda$  between 2.54 and 3.2 cm (1.0 and 1.25 in.). Again, there is a very rapid drop off in performance for  $\lambda > 3.3$  cm (1.3 in.). The similarity between the variation of  $\partial \bar{U} / \partial z)_{MAX}$  and  $\bar{\omega}_x$  with  $\lambda$  as embodied in Figs. 15 and 16, respectively, further underscores the important role played by the spanwise mean velocity gradient  $\partial \bar{U} / \partial z$  created by the PSVG array in the vorticity redistribution process.

The improvement in PSVG performance with increasing interelectrode spacing for  $\lambda < \lambda_{OPT}$  is associated with an increase in the (spanwise) extent of the plasma forming region on the dielectric surface and, hence, the associated body force for the range of applied voltages shown in Figs. 15 and 16. In other words, for applied voltages in the range of  $25 \text{ kV} \leq E_{pp} \leq 35 \text{ kV}$  and interelectrode spacings of  $\lambda = 1.27$  cm (0.5 in.) and  $1.91$  cm (0.75 in.), the region of surface plasma formation is artificially constrained in the spanwise extent, which, in turn, limits the body force and reduces the effectiveness of the actuator. In contrast, the loss of actuator effectiveness at interelectrode spacing  $\lambda < \lambda_{OPT}$  is due to a change in the character of the colliding spanwise wall jets associated with the plasma-induced flowfield, as shown in the PIV-based vorticity fields for the no-external-flow case shown Fig. 17. In particular, for  $\lambda = 1$  in., compact counter-rotating vortices are formed near the wall. In contrast, for  $\lambda = 1.5$  in., the formation of coherent surface vortices is significantly reduced.

The optimum value of spanwise interelectrode spacing for both  $(\partial \bar{U} / \partial z)_{MAX}$  and  $\bar{\omega}_x$  is approximately equal to the local 99% boundary-layer thickness on the plate upstream of the PSVG array. That is,  $\lambda_{OPT}/\delta \approx 1$ . The question naturally arises whether this is

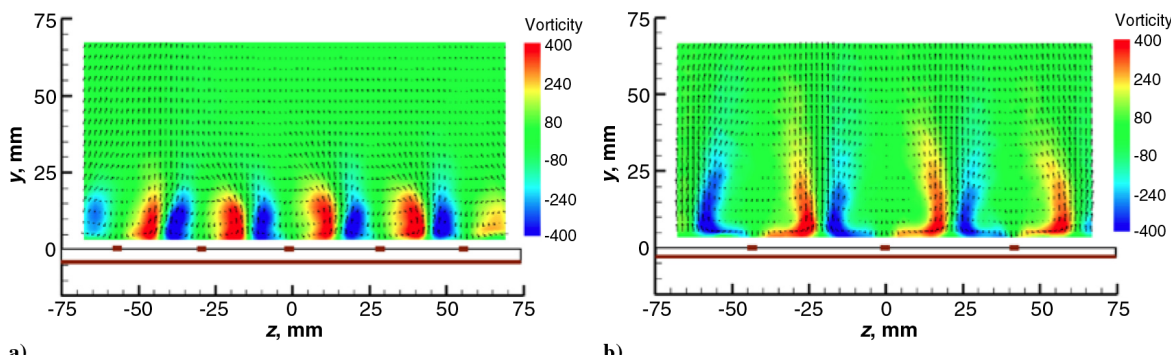


Fig. 17 Quiescent vorticity fields created by PSVG array with  $E_{pp} = 40$  kV and a)  $\lambda = 2.54$  cm (1 in.), and b)  $\lambda = 3.81$  cm (1.5 in.).

coincidental or whether the optimum spanwise interelectrode spacing actually scales with the approach boundary-layer thickness. To investigate this, the boundary layer upstream of the PSVG array was thickened by attaching a semicircular bump (15.9 mm in diameter) near the plate leading edge, followed by a downstream section of distributed surface roughness extending 10.2 cm in the streamwise direction. This passive treatment gave rise to a separation bubble followed by turbulent reattachment, which increased the turbulent boundary-layer thickness just upstream of the PSVG array by approximately 80%. The PSVG arrays with interelectrode spacing values  $\lambda = 1.905, 2.54, 3.18$ , and  $3.81$  cm (0.75, 1.0, 1.25, and 1.5 in., respectively) were again examined via LDA surveys to determine whether  $\lambda_{\text{OPT}}$  scaled with the new boundary-layer thickness  $\delta$ . In fact, results showed no change in the optimum electrode spacing, which confirms that its value is dictated solely by the physics of the plasma discharge process (i.e., the Maxwell's equations) and is decoupled from the approach boundary-layer flow.

#### IV. Conclusions

Measurements presented in this paper show that the body force associated with a PSVG array generates wall-normal mean vorticity through the creation of a spanwise mean velocity gradient  $\partial \bar{U} / \partial z$ . This vorticity is subsequently reoriented into the streamwise direction by the imposed boundary-layer mean strain rate  $\partial \bar{U} / \partial y$ . In a similar manner, the spanwise mean vorticity in the boundary layer  $\partial \bar{U} / \partial y$  is also reoriented into the streamwise direction by the actuator-induced spanwise mean velocity gradient  $\partial \bar{U} / \partial z$ . Thus, it is the product of mean strain rates  $(\partial \bar{U} / \partial y)(\partial \bar{U} / \partial z)$  that is important in the production of  $\bar{\omega}_x$  by the PSVG array. The interaction between the boundary layer and plasma-induced body force is shown to significantly augment the production of  $\bar{\omega}_x$  over that produced by the actuator in the absence of an external flow.

The streamwise vorticity production mechanism described earlier is quite different from that outlined by Jukes and Choi [13] for their single electrode plasma vortex generator. In that case, the plasma-induced spanwise wall jet outer shear layer contained more streamwise vorticity than the spanwise vorticity in the approach laminar boundary layer. As such, vorticity redistribution mechanisms, which are key in this study, did not play as prominent a role. It is also interesting to note that the maximum mean streamwise vorticity produced by the PSVG array in the current study was  $\bar{\omega}_{x,\text{MAX}} \delta / U \approx O(5000)$ , whereas that reported by Jukes and Choi [13] was  $\bar{\omega}_{x,\text{MAX}} \delta / U \approx O(10)$ .

Scaling arguments based on the mean vorticity transport equation show, and experiments confirm, that the streamwise mean vorticity produced by the array is proportional to both the external flow speed  $U_\infty$  (for fixed  $L$ ) and streamwise extent of the plasma forming region  $L$  (for fixed  $U_\infty$ ). For turbulent boundary layers, this scaling is expected to hold provided that  $T_C \geq S_{xz}^{-1}$ . Furthermore, the streamwise vorticity downstream of the actuator array is found to scale proportionately with the plasma-induced body force. Because the body force, in turn, scales with applied voltage to the  $7/2$  power, there is considerable advantage to be gained by operating the PSVG arrays at high voltages. This can be accomplished by the use of thick dielectric barriers, as described in Thomas et al. [14]. The optimum spanwise interelectrode spacing does not scale with the approach boundary-layer thickness. Instead, optimum  $\lambda$  is governed solely by the local plasma dynamics. For fixed applied voltage, if the interelectrode spacing is too small, the spanwise extent of the plasma forming region is artificially constrained, which reduces the body force and hence the ability to produce streamwise vorticity. For too large a spacing, the local upwelling produced by colliding spanwise wall jets is negatively affected, which in turn reduces the  $\partial \bar{U} / \partial z$  required for effective actuator performance.

#### Acknowledgments

This work was supported by Innovative Technology Applications Company, LLC under a Small Business Innovation Research Phase II Contract (N00014-11-C-0267) issued by the U.S. Department of the Navy. The authors would like to thank Judah Milgram and John Kinzer of the Office of Naval Research for their support and encouragement during this effort. The authors would also like to acknowledge Eras Noel for his important contributions to the data acquisition as well as many fruitful discussions with David Schatzman and Patrick Bowles.

#### References

- [1] Lin, L., "Review of Research on Low-Profile Vortex Generators to Control Boundary Layers," *Progress in Aerospace Sciences*, Vol. 38, Nos. 4–5, 2002, pp. 389–420.  
doi:10.1016/S0376-0421(02)00010-6
- [2] Bushnell, D., "Longitudinal Vortex Control-Techniques and Applications," *Aeronautical Journal*, Vol. 96, No. 958, Oct. 1992, pp. 293–312.
- [3] Martin, P. B., Wilson, J. S., Berry, J. D., Wong, T.-C., Moultron, M., and McVeigh, M. A., "Passive Control of Compressible Dynamic Stall," *Applied Aerodynamics Conference*, AIAA Paper 2008-7506, Aug. 2008.
- [4] Corke, T. C., Post, M. L., and Orlov, D.M., "Single Dielectric Barrier Discharge Plasma Enhanced Aerodynamics: Physics, Modeling and Applications," *Experiments in Fluids*, Vol. 46, No. 1, 2009, pp. 1–26.  
doi:10.1007/s00348-008-0582-5
- [5] Moreau, E., "Airflow Control by Non-Thermal Plasma Actuators," *Journal of Physics D: Applied Physics*, Vol. 40, No. 3, 2007, pp. 605–636.  
doi:10.1088/0022-3727/40/3/S01
- [6] Huang, X., Chan, S., and Zhang, X., "Atmospheric Plasma Actuator," *IEEE Transactions on Plasma Science*, Vol. 35, No. 3, 2007, pp. 693–695.  
doi:10.1109/TPS.2007.896781
- [7] Schatzman, D. M., and Thomas, F. O., "Turbulent Boundary Layer Separation Control Using Plasma Actuators," *AIAA Journal*, Vol. 48, No. 8, 2010, pp. 1620–1634.  
doi:10.2514/1.J050009
- [8] Kozlov, A. V., and Thomas, F. O., "Flow Control via Two Types of Dielectric Barrier Discharge Plasma Actuation," *AIAA Journal*, Vol. 49, No. 9, 2011, pp. 1919–1931.  
doi:10.2514/1.J050793
- [9] Kozlov, A. V., and Thomas, F. O., "Plasma Flow Control of Cylinders in a Tandem Configuration," *AIAA Journal*, Vol. 49, No. 10, 2011, pp. 2183–2193.  
doi:10.2514/1.J050976
- [10] Okita, Y., Jukes, T., Choi, K.-S., and Nakamura, K., "Flow Reattachment over an Airfoil Using Surface Plasma Actuator," AIAA Paper 2008-4203, 2008.
- [11] Jukes, T. N., Segawa, T., and Furutani, H., "Flow Control on a NACA 4412 Using Dielectric-Barrier-Discharge Vortex Generators," *AIAA Journal*, Vol. 51, No. 2, 2013, pp. 452–464.  
doi:10.2514/1.J051852
- [12] Jukes, T. N., and Choi, K.-S., "Dielectric Barrier-Discharge Vortex Generators: Characterization and Optimization for Flow Separation Control," *Experiments in Fluids*, Vol. 52, No. 2, 2012, pp. 329–345.  
doi:10.1007/s00348-011-1213-0
- [13] Jukes, T. N., and Choi, K.-S., "On the Formation of Streamwise Vortices by Plasma Vortex Generators," *Journal of Fluid Mechanics*, Vol. 733, Oct. 2013, pp. 370–393.  
doi:10.1017/jfm.2013.418
- [14] Thomas, F. O., Corke, T. C., Iqbal, M., Kozlov, A., and Schatzman, D., "Optimization of SDBD Plasma Actuators for Active Aerodynamic Flow Control," *AIAA Journal*, Vol. 47, No. 9, 2009, pp. 2169–2178.  
doi:10.2514/1.41588
- [15] Klebanoff, P. S., "Characteristics of Turbulence in a Boundary Layer with Zero Pressure Gradient," NACA TR-1247, 1955.

A. Naguib  
*Associate Editor*

# Technical Notes

## Effect of Relative Humidity on Dielectric Barrier Discharge Plasma Actuator Body Force

Michael Wicks\* and Flint O. Thomas†

University of Notre Dame, Notre Dame, Indiana 46556

DOI: 10.2514/1.J053810

### Nomenclature

$E$	=	electric field
$F_B$	=	actuator body force
$P$	=	pressure
$P_{SAT}$	=	saturated water vapor pressure
$P_V$	=	partial pressure of water vapor
$T$	=	reactive thrust
$T_{DRY}$	=	reactive thrust for $RH < 40\%$
$V_{PP}$	=	peak-to-peak applied voltage
$RH$	=	relative humidity
$\rho$	=	moist air density
$\rho_C$	=	charge density
$\rho_{dry}$	=	dry air density

### I. Introduction

THE efficacy of dielectric barrier discharge (DBD) plasma actuators for aerodynamic flow control has been demonstrated in numerous studies as described in recent reviews on the subject by Corke et al. [1,2] and Moreau [3]. Most studies have been performed under well-controlled laboratory environmental conditions. However, application of these devices for active flow control on aircraft will require their effective operation over a wide range of climate conditions. Because the aerodynamic benefit of the devices is increasingly well (if not completely) understood, it is timely to investigate and characterize environmental influences that could potentially limit their utility. This Note focuses on the influence of ambient relative humidity (RH) on the body force produced by DBD plasma actuators. Although it is generally recognized that the efficacy of DBD actuators is reduced with increased relative humidity, the functional variation of actuator reactive thrust (a quantity directly proportional to body force) with relative humidity needs to be quantified. Determination of the functional variation of the body force with relative humidity would enable the development of DBD actuator compensator circuits for use on aircraft.

There have been previous efforts to assess the influence of relative humidity on DBD actuator performance. Anderson and Roy [4] reported preliminary experiments assessing the effect of relative humidity on the surface pressure coefficient over the somewhat

Received 20 August 2014; revision received 6 April 2015; accepted for publication 14 May 2015; published online 28 July 2015. Copyright © 2015 by the American Institute of Aeronautics and Astronautics, Inc. All rights reserved. Copies of this paper may be made for personal or internal use, on condition that the copier pay the \$10.00 per-copy fee to the Copyright Clearance Center, Inc., 222 Rosewood Drive, Danvers, MA 01923; include the code 1533-385X/15 and \$10.00 in correspondence with the CCC.

\*Graduate Research Assistant, Department of Aerospace & Mechanical Engineering, Institute for Flow Physics and Control. Member AIAA.

†Professor, Department of Aerospace & Mechanical Engineering, Institute for Flow Physics and Control. Associate Fellow AIAA.

narrow range of  $43\% \leq RH \leq 53\%$ . They suggested a modest increase in actuator performance with relative humidity. A more recent study was reported by Benard et al. [5] over a wider range of  $40\% \leq RH \leq 98\%$ . The actuator used a sinusoidal ac frequency of 1 kHz and voltage amplitudes from 16 to 24 kV. Although the results showed that DBD actuators can be operated at high RH, the measured plasma-induced wall jet velocity was clearly reduced with increased RH. The effect of RH on actuator thrust was not documented. The authors also examined the effect of RH on current discharge characteristics and noted that the number of positive and negative current peaks generally decreased with increased RH.

Ashpis and Laun [6] performed a systematic investigation to address the apparent nonrepeatability of thrust measurements made with DBD plasma actuators. Their focus was to develop a more reliable method for measuring DBD actuator thrust. In the course of their investigation, they performed measurements at two fixed relative humidity values: a “low” value of  $RH = 18\%$  and a “humid” case of  $RH = 50\%$ . They show that increasing relative humidity reduces measured thrust. However, with only two RH values, the functional form of the variation was obviously not determined.

In this study, the effect of RH on the reactive thrust produced by a DBD plasma actuator is systematically investigated. The performance metric of reactive thrust is directly proportional to the actuator-induced body force  $F_B = \rho_C E$  and was measured directly by a procedure similar to that used in the plasma actuator optimization study of Thomas et al. [7]. Although the reactive thrust is only proportional to body force, this is sufficient for the purposes of this study because it is the characterization of the change in  $F_B$  with RH that is of interest here. Furthermore, results are presented for a wide range of relative humidity,  $20\% \leq RH \leq 90\%$ , and for peak-to-peak applied voltages up to 50 kV. Details regarding the experimental facility are presented in the following section.

### II. Experimental Apparatus

As shown in the schematic of Fig. 1, the experimental facility consists of a closed, rectangular test chamber of dimensions 2 m in length and 0.61 m square in cross section (an enclosed volume of  $0.74 \text{ m}^3$ ). This size was sufficient to prevent the actuator from inducing large-scale recirculating flow inside the chamber. To control the RH level, a Hamilton Beach True Air Ultrasonic Humidifier was installed inside the closed chamber. The humidifier produced droplets with a median diameter of approximately  $2 \mu\text{m}$ . The chamber was instrumented with two Honeywell type HIH-4031 RH sensors located on either side of the plasma actuator. These were used for real-time monitoring of the RH inside the chamber. The estimated relative uncertainty of the RH measurement was  $\pm 3.8\%$  at 95% confidence. A Vishay NTC thermistor was used to correct the RH for temperature. The reactive thrust from the DBD plasma actuator was measured directly using the same method described in the actuator optimization study by Thomas et al. [7]. The instantaneous thrust produced by the DBD actuator was read directly from the display of an Acculab ALC force balance, which has a resolution of 0.098 mN (0.01 g), whereas RH and temperature readings were made using a Vernier LabQuest data-acquisition system. The relative uncertainty in the thrust measurement was  $\pm 4.0\%$  at 95% confidence. To examine lower-than-ambient humidity levels, an Sunpentown (SPT) SD-40E dehumidifier was added to the experimental arrangement shown in Fig. 1. This allowed the RH to be systematically varied over the nominal range of  $20\% \leq RH \leq 90\%$ .

The plasma actuator electrodes were constructed from Copper foil tape of 0.04 mm thickness mounted directly on a 0.318-cm-thick quartz plate dielectric surface. There was zero overlap between the exposed and covered electrodes. The length of the exposed and

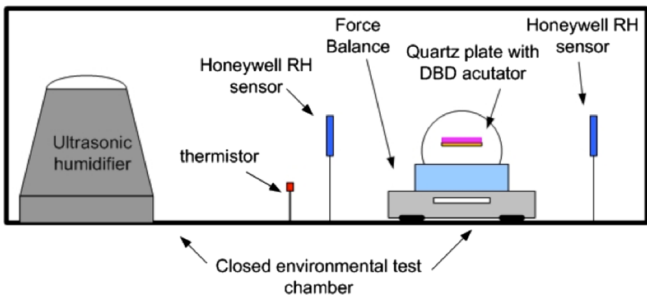


Fig. 1 Schematic of the experimental apparatus.

covered electrodes was 2.54 and 5.08 cm, respectively. The spanwise length of both electrodes was 20.32 cm. The top edge of the exposed electrode and the entire covered electrode were overlayed with two layers of 0.762-mm-thick high-voltage tape (3M Scotch 130C) to avoid the formation of plasma at the edge and rear, respectively. The circuit used to operate the DBD actuator is identical to that presented in figure 6 of Kozlov and Thomas [8]. The plasma actuator was operated with a sinusoidal ac voltage with peak-to-peak amplitude varying from 35 to 50 kV and ac frequency of 2 kHz.

The plasma actuator was oriented such that the resulting plasma-induced flow was directed upward (away from the force balance), and so the reactive thrust acting downward was measured directly by the balance. A block of lightweight insulating foam material supported the actuator. This is also shown schematically in Fig. 1. The leads that power the actuator used thin wires that were not under tension, and so they had no influence on the thrust measurements. The force balance was enclosed in a Faraday cage to minimize electromagnetic noise influencing the force measurements. This procedure was verified by positioning the balance with a fixed, known weight in the vicinity of an operating plasma actuator. The presence of plasma had no influence on the weight measurement.

### III. Experimental Results

Within experimental uncertainty, it was found that the reactive thrust produced by the DBD actuator was essentially constant for  $RH < 40\%$ . In the subsequent discussion, we will denote these (constant) actuator thrust values measured for  $RH < 40\%$  as  $T_{DRY}$ . For the range of applied voltages used in this investigation ( $35 \leq V_{PP} \leq 50$  kV), it was observed that  $T_{DRY} \propto V^{2.3}$ , a result fully consistent with figure 5 of Thomas et al. [7].

For  $RH > 40\%$  a systematic reduction in actuator thrust occurs and is found to be well represented by a power law of form

$$\left( \frac{T_{DRY} - T}{T_{DRY}} \right) = \alpha \left( \frac{P_V}{P_{SAT}} \right)^\beta \quad (1)$$

where  $\alpha$  and  $\beta$  are constant for a given applied voltage. An example of this power-law variation for the humidity-induced reduction of reactive thrust is shown in Fig. 2 for the case of  $V_{PP} = 35$  kV. The linear variation shown on this log-log plot clearly indicates that the actuator thrust reduction with relative humidity follows a power law with exponent  $\beta = 4.1$ .

Figure 3 presents the measured reduction in reactive thrust with  $RH$  for the 40 kV case. Again, a log-log scale is used, which clearly indicates a power-law variation of the thrust reduction with  $RH$ . Note, however, that for  $RH > 70\%$  the power-law exponent is reduced. The reduction in power-law exponent commencing near  $RH = 70\%$  was also observed for the 45 and 50 kV cases as well. A comparison of Figs. 2 and 3 shows that the exponent characterizing the initial power-law variation has changed. In fact, our measurements clearly indicate that the power-law exponents are a function of the applied actuator voltage, although the function form [Eq. (1)] is not. This becomes readily apparent from Fig. 4, which presents the thrust reduction measurements for the 45 kV case. Note that the initial reduction in actuator thrust follows a power law with  $\beta_1 = 8.9$ . For  $RH > 70\%$ , the power-law exponent is reduced to  $\beta_2 = 6.3$ , and it is interesting to

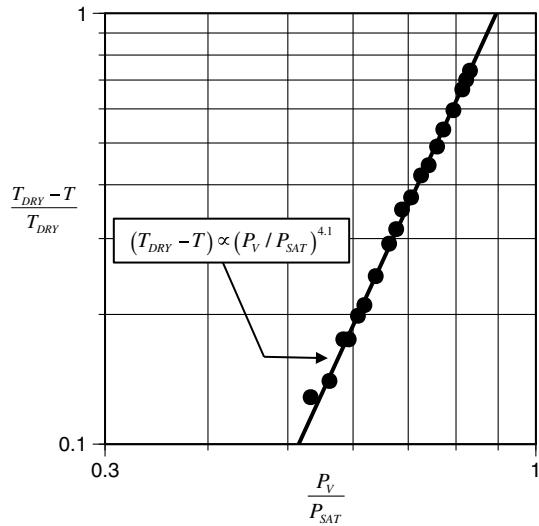


Fig. 2 Measured power-law reduction in actuator thrust for the 35 kV case.

note that the ratio of the power-law exponents in the two regimes shown in Figs. 3 and 4 (as well as for the 50 kV case) is a constant,  $\beta_1/\beta_2 \approx 1.4$ . The functional variation of the power-law exponents  $\beta_1$  and  $\beta_2$  with applied voltage is shown in the inset to Fig. 4.

One may question whether the reduction in thrust shown in the previous figures may be simply due to a reduction in air density associated with increased RH. It is easy to show that the density of the air in the chamber,  $\rho$ , as a function of RH is given by

$$\rho = \rho_{DRY} \left( 1 - RH \frac{P_{SAT}}{P} \right) \quad (2)$$

where  $\rho_{DRY}$  is the dry air density,  $P_{SAT}$  is the saturation water vapor pressure, and  $P$  is the ambient pressure. Equation (2) expresses the well-known fact that air density is reduced with increased relative humidity. Substitution of values consistent with the reported experiments into Eq. (2) shows that, for a relative humidity of 90%,  $\rho/\rho_{DRY} \approx 0.97$ , so that one would expect only a 3% reduction in thrust for the highest RH tested (if solely due to reduced density). This is far smaller than the thrust reductions shown in Figs. 2–4, which approach 70%. Furthermore, the reduction in reactive thrust with RH is nonlinear. Equation (2) predicts a linear variation, which is not the case. It is clear from the measurements that the reduction in actuator thrust is not due to a simple density effect.

Figure 5 presents photographs of the DBD plasma actuator discharge for three representative applied voltage cases. Two images

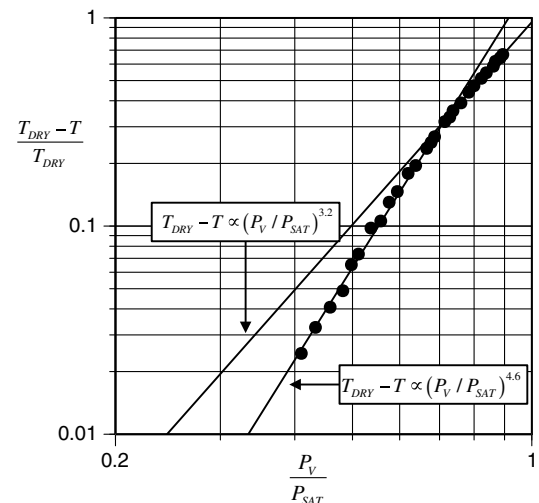


Fig. 3 Measured power-law reduction in actuator thrust for the 40 kV case. Note that the power-law exponent changes for  $RH > 70\%$ .

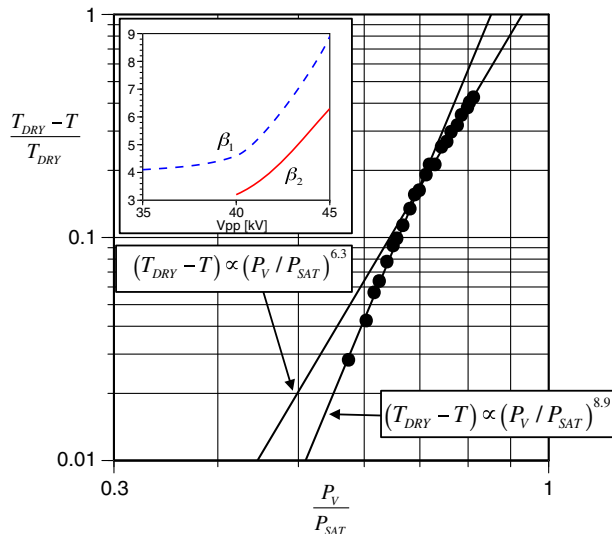


Fig. 4 Measured power-law reduction in actuator thrust for the 45 kV case. Inset: functional variation of  $\beta_1$  and  $\beta_2$  with applied voltage for the range of the experiments.

are shown at each applied voltage. The first shows the discharge at ambient relative humidity ( $RH = 40\%$ ) where negligible thrust reduction is observed and the second at a comparatively high relative humidity ( $RH = 75\%$ ). It is apparent that the character of the discharge is markedly changed with increased relative humidity. In particular, Fig. 5 shows a glow discharge that is typical of DBD plasma actuators for each of the  $RH = 40\%$  cases. In contrast, at  $RH = 75\%$ , the discharge is infused with multiple discrete filamentary streamers, with the effect most apparent in the two highest applied voltage cases. Photographic evidence shows that the reduction in thrust at increased RH appears associated with the transition from glow discharge to filamentary discharge. At lower actuator voltages, this transition is gradual but it is more sudden at the highest voltages like the 50 kV case. Koo et al. [9] investigated the effect of moisture content on the spatial uniformity of a 13.56 MHz RF-powered dielectric barrier discharge using helium gas. Their study showed that, as the moisture content increased, the character of the discharge changed from uniform glow to streak discharge which is consistent with the results shown in Fig. 5. Figure 6 compares images of the actuator discharge for the experiment with  $V_{PP} = 40$  kV (corresponding to the thrust measurements shown in Fig. 3). At below-ambient  $RH = 15\%$ , a uniform glow discharge is observed, but at  $RH = 85\%$ , the plasma is dominated by discrete streamers.

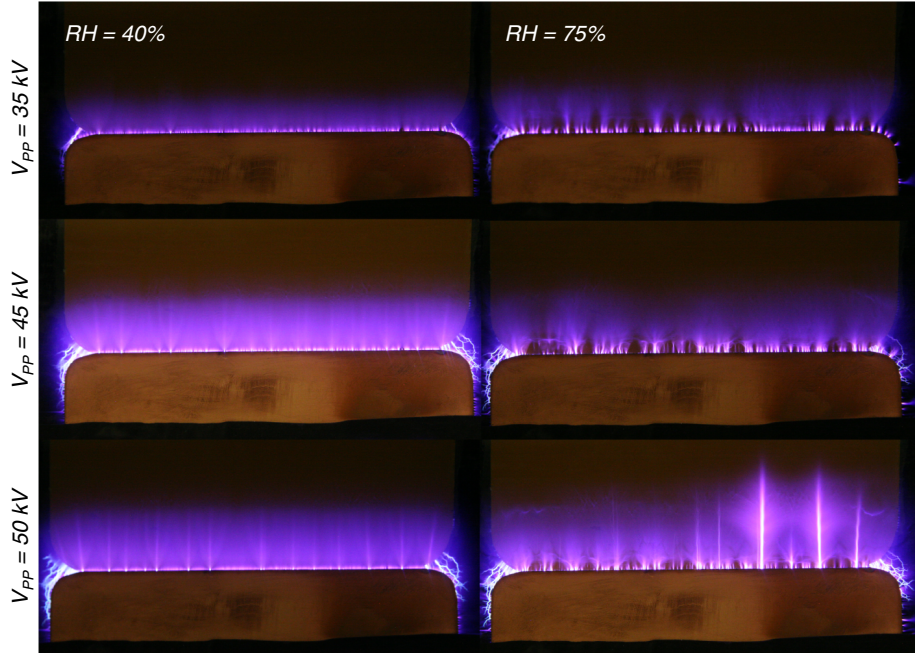


Fig. 5 Photographs of the DBD discharge at ambient and high RH.

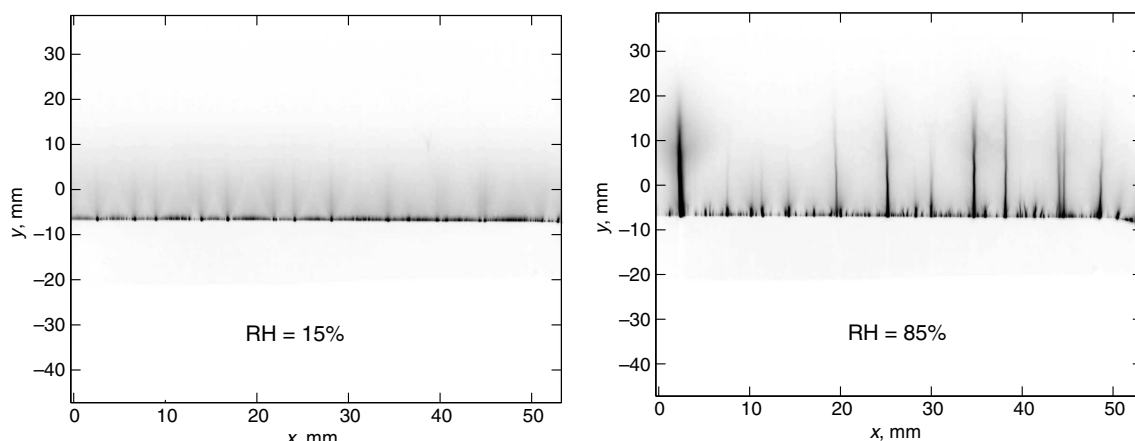


Fig. 6 Photographs comparing the DBD discharge for below-ambient and high RH;  $V_{PP} = 40$  kV.

Measurements show that the integrated light emission at high humidity is an order-of-magnitude larger than at low humidity.

It was shown in [7] that, at the highest applied voltages used in DBD plasma actuators, discrete filamentary structures (streamers) developed in the plasma that resemble those shown in Figs. 5 and 6 (see figure 8 of [7] for a comparison). It was shown that, once discrete streamer formation occurred, further increases in applied voltage did not result in a significant increase in the reactive thrust (body force) but dissipated power increased sharply. Because the onset of streamer formation is associated with maximum thrust and an increase in dissipated power, this was referred to as the actuator saturation condition. A focus of [7] was to achieve higher DBD actuator authority by delaying actuator saturation to higher applied voltages. This was achieved by using comparatively thick dielectric barrier materials with low dielectric constant. Together, these functioned to lower the effective capacitance of the actuator, which had the effect of lowering the surface charge density at fixed applied voltage.

Figures 5 and 6 indicate that the effect of increasing RH at fixed applied voltage is to promote discrete streamer formation, thereby lowering the reactive thrust (body force). It is conjectured that this effect is associated with a humidity-induced modification of the charge distribution on the dielectric surface, giving rise to spatial inhomogeneity that reduces the number of microdischarges and promotes discrete streamer formation at preferred locations. This is in contrast to the homogeneous distribution of numerous microdischarges over the dielectric surface that characterizes the glow discharge regime [10]. In addition, it should be acknowledged that plasma chemistry could also play a role in the body force reduction. For example, Kim et al. [11] presented experimental results that indicated the importance of oxygen and oxygen negative ions in the body force produced by DBD plasma actuators. In humid air, the plasma chemistry can be modified to reduce the body force through the creation of active species such as OH and H<sub>2</sub>O<sub>2</sub>.

#### IV. Conclusions

Based upon the results of this investigation, it is found that the reduction in reactive thrust produced by the actuator is negligible for RH < 40%. For higher levels of relative humidity, a very significant reduction (approaching 70% in this study) in the actuator-induced thrust is observed. More importantly, the functional variation of thrust reduction with relative humidity is well approximated by a power law in the form of Eq. (1). The power-law exponent is observed to increase with applied voltage. In addition, for the applied voltage cases greater than V<sub>PP</sub> = 35 kV, the power-law exponent is reduced for RH > 70%. Denoting the power-law exponent for 40% ≤ RH ≤ 70% as  $\beta_1$  and that for RH > 70% as  $\beta_2$ , it was found that, in each case,  $\beta_1/\beta_2 \approx 1.41$ . Based upon photographs of the discharge at each applied voltage, and for both low and high relative humidity conditions, it is conjectured that the change in power-law exponent for RH > 70% is associated with a reduction in number of microdischarges and the transition to the formation of discrete streamers.

Knowledge of the functional variation of dielectric barrier discharge (DBD) actuator thrust reduction with relative humidity (RH) provides important information required for the design of actuator humidity compensation circuits. Using such a unit, the detrimental effect of RH can be fully compensated by increasing the actuator operating voltage by the appropriate amount. Of course, this presumes that the dielectric material and thickness as well as ac frequency is suitable for operating at the required elevated voltages

without transitioning to the filamentary discharge regime observed in [7]. One can envision in-flight measurement of RH with similar small, solid-state RH sensors as used in these experiments. With RH determined, and the functional dependence on actuator thrust known a priori, the DBD-actuator operating voltages could be automatically increased by a previously prescribed amount to fully compensate for any RH induced performance loss.

Future work should focus on the mechanism of filament formation at high RH, which may provide insight into the design of dielectric materials/surfaces more suitable for high-RH environments.

Finally, it should be noted that the generality of power-law relation (1) remains an open question. It remains to be determined whether the functional reduction in reactive thrust with RH as documented in this Note can be generalized to other DBD actuator geometric configurations.

#### References

- [1] Corke, T. C., Post, M. L., and Orlov, D. M., "Single Dielectric Barrier Discharge Plasma Enhanced Aerodynamics: Physics, Modeling and Applications," *Experiments in Fluids*, Vol. 46, No. 1, 2009, pp. 1–26. doi:10.1007/s00348-008-0582-5
- [2] Corke, T. C., Enlo, C. L., and Wilinson, S. P., "Dielectric Barrier Discharge Plasma Actuators for Flow Control," *Annual Review of Fluid Mechanics*, Vol. 42, No. 1, 2010, pp. 505–529. doi:10.1146/annurev-fluid-121108-145550
- [3] Moreau, E., "Airflow Control by Non-Thermal Plasma Actuators," *Journal of Physics D: Applied Physics*, Vol. 40, No. 3, 2007, pp. 605–636. doi:10.1088/0022-3727/40/3/S01
- [4] Anderson, R., and Roy, S., "Preliminary Experiments of Barrier Discharge Plasma Actuators Using Dry and Humid Air," *44th AIAA Aerospace Sciences Meeting and Exhibit*, AIAA Paper 2006-0369, Jan. 2006.
- [5] Benard, N., Balcon, N., and Moreau, E., "Electric Wind Produced by a Surface Dielectric Barrier Discharge Operating over a Wide Range of Relative Humidity," *47th AIAA Aerospace Sciences Meeting*, AIAA Paper 2009-0488, Jan. 2009.
- [6] Ashpis, D. E., and Laun, M. C., "Dielectric Barrier Discharge Actuators Thrust-Measurement Methodology Incorporating New Anti-Thrust Hypothesis," *52nd Aerospace Sciences Meeting*, AIAA Paper 2014-0486, 2014.
- [7] Thomas, F. O., Corke, T. C., Iqbal, M., Kozlov, A., and Schatzman, D., "Optimization of Dielectric Barrier Discharge Plasma Actuators for Active Aerodynamic Flow Control," *AIAA Journal*, Vol. 47, No. 9, 2009, pp. 2169–2178. doi:10.2514/1.J051588
- [8] Kozlov, A. V., and Thomas, F. O., "Flow Control via Two Types of Dielectric Barrier Discharge Plasma Actuation," *AIAA Journal*, Vol. 49, No. 9, 2011, pp. 1919–1931. doi:10.2514/1.J050793
- [9] Koo, I. G., Cho, J. H., and Woong, M. L., "Influence of the Gas Humidity on the Uniformity of RF-Powered-Atmospheric Pressure Low-Temperature DBD Plasmas," *Plasma Process Polymers*, Vol. 5, No. 2, 2008, pp. 161–167. doi:10.1002/ppap.200700068
- [10] Fridman, A., and Kennedy, L. A., *Plasma Physics and Engineering*, Taylor and Francis, Philadelphia, 2004, pp. 574–579.
- [11] Kim, W., Do, H., Mungal, G., and Cappelli, M. A., "On the Role of Oxygen in Dielectric Barrier Discharge Actuation of Aerodynamic Flows," *Applied Physics Letters*, Vol. 91, No. 18, 2007, Paper 181501. doi:10.1063/1.2803755

A. Naguib  
Associate Editor

*This document was prepared & typeset with pdfL<sup>A</sup>T<sub>E</sub>X, and formatted with  
NDdiss2<sub>ε</sub> classfile (v3.2013[2013/04/16]) provided by Sameer Vijay and updated  
by Megan Patnott.*